Surface studies of limestones and dolostones: characterisation using various techniques and batch dissolution experiments with hydrochloric acid solutions

Lauri Järvinen

Geology and Mineralogy
Faculty of Science and Engineering
Åbo Akademi University
Åbo, Finland, 2015

Surface studies of limestones and dolostones: characterisation using various techniques and batch dissolution experiments with hydrochloric acid solutions

Lauri Järvinen

Geology and Mineralogy
Faculty of Science and Engineering
Åbo Akademi University
Åbo, Finland, 2015

Supervisors

Professor Olav Eklund
Geology and Mineralogy
Faculty of Science and Engineering
Åbo Akademi University
Domkyrkotorget 1, 20500 Åbo
Finland

Docent Jarkko Leiro
Materials Science
Department of Physics and Astronomy
University of Turku, 20014 Turku
Finland

Reviewers

Professor Alvar Soesoo
Chair of Physical Geology
Institute of Geology at Tallinn University of Technology
Ehitajate tee 5, 19086 Tallinn
Estonia

Professor Svante Svensson
Molecular and Condensed Matter Physics
Department of Physics and Astronomy
Uppsala University
Box 516, 751 20 Uppsala
Sweden

Opponent

Professor Alvar Soesoo
Chair of Physical Geology
Institute of Geology at Tallinn University of Technology
Ehitajate tee 5, 19086 Tallinn
Estonia

Layout: Pia Sonck-Koota
(www.sonck-koota.fi)

ISBN 978-952-12-3161-2
Painosalama Oy – Turku, Finland 2015

Abstract

In this thesis, stepwise titration with hydrochloric acid was used to obtain chemical reactivities and dissolution rates of ground limestones and dolostones of varying geological backgrounds (sedimentary, metamorphic or magmatic). Two different ways of conducting the calculations were used: 1) a first order mathematical model was used to calculate extrapolated initial reactivities (and dissolution rates) at *pH* 4, and 2) a second order mathematical model was used to acquire integrated mean specific chemical reaction constants (and dissolution rates) at *pH* 5. The calculations of the reactivities and dissolution rates were based on rate of change of *pH* and particle size distributions of the sample powders obtained by laser diffraction. The initial dissolution rates at *pH* 4 were repeatedly higher than previously reported literature values, whereas the dissolution rates at *pH* 5 were consistent with former observations. Reactivities and dissolution rates varied substantially for dolostones, whereas for limestones and calcareous rocks, the variation can be primarily explained by relatively large sample standard deviations. A list of the dolostone samples in a decreasing order of initial reactivity at *pH* 4 is:

1) metamorphic dolostones with calcite/dolomite ratio higher than about 6%
2) sedimentary dolostones without calcite
3) metamorphic dolostones with calcite/dolomite ratio lower than about 6%

The reactivities and dissolution rates were accompanied by a wide range of experimental techniques to characterise the samples, to reveal how different rocks changed during the dissolution process, and to find out which factors had an influence on their chemical reactivities. An emphasis was put on chemical and morphological changes taking place at the surfaces of the particles via X-ray Photoelectron Spectroscopy (XPS) and Scanning Electron Microscopy (SEM). Supporting chemical information was obtained with X-Ray Fluorescence (XRF) measurements of the samples, and Inductively Coupled Plasma-Mass Spectrometry (ICP-MS) and Inductively Coupled Plasma-Optical Emission Spectrometry (ICP-OES) measurements of the solutions used in the reactivity experiments. Information on mineral (modal) compositions and their occurrence was provided by X-Ray Diffraction (XRD), Energy Dispersive X-ray analysis (EDX) and studying thin sections with a petrographic microscope. BET (Brunauer, Emmet, Teller) surface areas were determined from nitrogen physisorption data. Factors increasing chemical reactivity of dolostones and calcareous rocks were found to be sedimentary origin, higher calcite concentration and smaller quartz concentration. Also, it is assumed that finer grain size and larger BET surface areas increase the reactivity although no certain correlation was found in this thesis. Atomic concentrations did not correlate with the reactivities. Sedimentary dolostones, unlike metamorphic ones, were found to have porous surface structures after dissolution.

In addition, conventional (XPS) and synchrotron based (HRXPS) X-ray Photoelectron Spectroscopy were used to study bonding environments on calcite and dolomite surfaces. Both samples are insulators, which is why neutralisation measures such as electron flood gun and a conductive mask were used. Surface core level shifts of 0.7 ± 0.1 eV for Ca 2p spectrum of calcite and 0.75 ± 0.05 eV for Mg 2p and Ca 3s spectra of dolomite were obtained. Some satellite features of Ca 2p, C 1s and O 1s spectra have been suggested to be bulk plasmons. The origin of carbide bonds was suggested to be beam assisted interaction with hydrocarbons found on the surface.

The results presented in this thesis are of particular importance for choosing raw materials for wet Flue Gas Desulphurisation (FGD) and construction industry. Wet FGD benefits from high reactivity, whereas construction industry can take advantage of slow reactivity of carbonate rocks often used in the facades of fine buildings. Information on chemical bonding environments may help to create more accurate models for water-rock interactions of carbonates.

Sammanfattning

I denna doktorsavhandling användes stegvis titrering med saltsyra för att uppmäta kemiska reaktiviteter och hur snabbt man löser upp malda kalkstensprover och dolomitstensprover med olika geologiska ursprung (sedimentära, metamorfa eller magmatiska). Beräkningarna utfördes på två sätt: 1) en förstagradsmatematisk modell användes för att räkna ut extrapolerade initiala reaktiviteter (och upplösningshastigheter) vid *pH* 4, och 2) en andragrads matematisk modell användes för att räkna ut integrerade genomsnittliga specifika kemiska reaktionskonstanter (och upplösningshastigheter) vid *pH* 5. Uträkningarna av reaktiviteter och upplösningshastigheter baserade sig på förändringshastigheten i *pH* och partikelstorlekfördelningar. De senareuppmättes med laserdiffraktion. De initiala upplösningshastigheterna vid *pH* 4 var i upprepade experiment större än tidigare publicerade värden, medan upplösningshastigheterna vid *pH* 5 liknade de som tidigare publicerats. Reaktiviteterna och upplösningshastigheterna varierade mycket för dolomitstenar, men inte för kalkstenar och kalkhaltiga stenar. Variationerna för kalkstenarna och de kalkhaltiga stenarna kan förklaras med hjälp av relativt stora standardavvikelser i uppmätta värden. Dolomitstenarnas initiala reaktiviter vid *pH* 4 kan ordnas i nedåtgående ordning:

1) metamorfa dolomitstenar som innehåller mera än ungefär 6 % kalcit
2) sedimentära dolomitstenarsom inte innehåller kalcit
3) metamorfa dolomitstenar som innehåller mindre än ungefär 6 % kalcit

Reaktiviteterna och upplösningshastigheterna kompletterades med flera experimentella metoder för att karakterisera proverna, utreda hur olika stenar förändrar sig under lösningsprocessen och utreda vilka faktorer som påverkar stenarnas kemiska reaktiviteter. Kemiska och morfologiska förändringar på provernas ytor erhölls genom att använda X-ray Photoelectron Spectroscopy (XPS) och Scanning Electron Microscopy (SEM). X-Ray Fluorescence (XRF) användes för att erhålla provernas kemiska sammansättningar, och Inductively Coupled Plasma-Mass Spectrometry (ICP-MS) och Inductively Coupled Plasma-Optical Emission Spectrometry (ICP-OES) för att mäta kemiska sammansättningar från lösningarna i reaktivitetexperimenten. Information om de modala kompositionerna erhölls med X-Ray Diffraction (XRD), och Energy Dispersive X-ray analysis (EDX), och undersökningar av tunnslip med ett petrografiskt mikroskop. BET- (Brunauer, Emmet, Teller) ytor bestämdes via kvävets fysisorptionsdata. Ett sedimentärt ursprung, en högre kalsitkonsentration och en lägre kvartskonsentration ökade den kemiska reaktiviteten av dolomitstenar och kalkhaltiga stenar. Härutöver, kan

det antas att en mindre kornstorlek och större BET-yta kan öka reaktivitet även om en säker korrelation inte kunde påvisas. Elementhalterna korrelerade inte med reaktiviteterna. Till skillnad från de metamorfa dolomitstenarna hade de sedimentära dolomitstenarna porösa ytor efter upplösningen.

Härutöver användes X-ray Photoelectron Spectroscopy (XPS) och synkrotronljus baserad (HRXPS) X-ray Photoelectron Spectroscopy för att studera de kemiska bindningarna på kalsit- och dolomitytorna. Båda proverna är icke-ledande, och därför användes en elektronflödeskanon med en ledande mask för neutralisering av ytorna. Kemiska ytskift på 0,7 ± 0,1 eV uppmättes i Ca 2p spektrum av kalcit och 0,75 ± 0,05 eV i Mg 2p och Ca 3s spektra av dolomit. Några satelliter i Ca 2p, C 1s och O 1s spektra föreslogs härröra från bulk plasmoner. Ursprunget till karbidbindningarna föreslogs vara interaktionen mellan elektronstrålen och kolvätet på ytan.

Resultaten som presenteras i denna doktorsavhandling kan utnyttjas av byggnadsindustrin, och kolkraftverk som vill ta bort svavel ur (desulfurisera) förbränningsgaserna. Våt desulfurisering av förbränningsgas har större nytta av en hög reaktivitet medan byggnadsindustrin har större nytta av en lägre reaktivitet för karbonatstenens yta, då dessa ofta används i fasader. Information om de kemiska bindningarna bidrar till att skapa noggrannare modeller för växelverkan mellan vatten och karbonatytan.

List of Abbreviations and Symbols

Abbreviations

AFM	Atomic Force Microscopy	
BET	Brunauer Emmet Teller	
DFT	Density Functional Theory	
EDX	Energy Dispersive X-ray analysis	
EDXRF	Energy Dispersive X-Ray Fluorescence	
ESCA	Electron Spectroscopy for Chemical Analysis	
FGD	Flue Gas Desulphurisation	
FTIR	Fourier Transform Infrared spectroscopy	
FWHM	Full Width at Half Maximum	
HRXPS	High Resolution X-ray Photoelectron Spectroscopy	(figs. 22, 26)
ICP	Inductively Coupled Plasma	
ICP-AES	Inductively Coupled Plasma-Atomic Emission Spectrometry	
ICP-MS	Inductively Coupled Plasma-Mass Spectrometry	
ICP-OES	Inductively Coupled Plasma-Optical Emission Spectrometry	
MED	Mean Escape Depth	
rf	Radio frequency	
SCLS	Surface Core Level Shift	
SCM	Surface Complexation Model	
SEM	Scanning Electron Microscopy	
TEM	Transmission Electron Microscope	
TST	Transition State Theory	
UHV	Ultra High Vacuum	
VSI	Vertical Scanning Interferometry	
WDXRF	Wavelength Dispersive X-Ray Fluorescence	
XPS	X-ray Photoelectron Spectroscopy	(fig. 26)
XRD	X-Ray Diffraction	
XRF	X-Ray Fluorescence	

Chemical species

Al_2O_3	Aluminium oxide	(table 2)
Ca^{2+}	Calcium ion	(equs. 2, 3, 4, 6, fig. 6)
CaC_2	Calcium carbide	
$CaCO_3$	Calcium carbonate, calcite, aragonite	(equs. 1, 2, 3, 4, 14, 31)
$CaCl_2$	Calcium chloride	
$CaMg(CO_3)_2$	Dolomite	(equ. 6)
CaO	Calcium oxide, burnt lime	(table 2)
$CaSO_4$	Calcium sulphate, anhydrite	
$CaSO_4 \cdot 2H_2O$	Gypsum	(equ. 1)

CO_2	Carbon dioxide	(equs. 1, 6, fig. 3)
CO_3^{2-}	Carbonate ion	(fig. 6)
CO_3	Carbonate molecule	(table 5, fig. 24)
CO_3H	Protonated carbonate	(equ. 5)
Fe_2O_3	Iron (III) oxide	(table 2)
H^+	Hydrogen ion, proton	(equs. 2, 6, 8, 30)
H_2CO_3	Carbonic acid	(equ. 3)
H_2SO_4	Sulphuric acid	
HCl	Hydrochloric acid	
HCO_3^-	Bicarbonate ion, hydrogen carbonate ion	(equs. 2, 3, 4)
K_2O	Potassium oxide	(table 2)
LaB_6	Lanthanum hexaboride	
Me	Divalent metal	(equ. 5)
$MeOH_2^+$	Protonated metal	(equ. 5)
Mg^{2+}	Magnesium ion	(equ. 6, fig. 6)
$MgCO_3$	Magnesium carbonate, magnesite	
MgO	Magnesium oxide	(table 2)
MnO	Manganese oxide	(table 2)
N_2	Nitrogen gas	
Na_2O	Sodium oxide	(table 2)
O_2	Oxygen gas	(equ. 1)
OH^-	Hydroxide ion	(equ. 4)
P_2O_5	Phosphorus pentoxide	(table 2)
SiO_2	Silicon dioxide	(table 2)
SO_2	Sulphur dioxide	(equ. 1)
SrO	Strontium oxide	(table 2)
TiO_2	Titanium dioxide	(table 2)
W	Tungsten	

Variables

a	Activity of a chemical species	(equ. 7)
A	Surface area (m^2)	(equs. 11, 13)
A_x	Cross-sectional adsorbate area	(equ. 29)
c	Mass concentration of particles in suspension(kg/m^3)	(equs. 11, 13)
C	Molar concentration (kmol/m^3)	(equs. 14, 16, 32)
C_x	Atomic concentration of element x in a sample	(equ. 22)
d	Thickness of a surface layer	(equ. 23)
d	Distance between atomic planes	(equ. 27, fig. 15)
d_i	Average size of particles in size range i (m)	(equs. 11, 12, 13)
d_s	Anion-cation distance	(equ. 20)
D_{H^+}	Diffusivity of the hydrogen ion in water (m^2/s)	(equs. 11, 12)
E	Energy	(equs. 24, 25, 26, fig. 9)

E	Electric field	(fig. 11)
E_0	Position (energy) of a specific peak	(equs. 24, 25)
E_A	Kinetic energy	(fig. 10)
E_b	Binding energy	(equs. 17, 18, 19)
E_c^b	Binding energy of bulk atoms	(equ. 20)
E_c^s	Binding energy of surface atoms	(equ. 20)
$E_\mathrm{f}(\mathrm{n} - 1)$	Final state energy	(equ. 18)
$E_\mathrm{i}(\mathrm{n})$	Initial state energy	(equ. 18)
E_k	Kinetic energy of a photoelectron	(equ. 17)
E_pass	Pass energy of an analyser	(table 3)
fR	Remaining mass fraction ()	(equs. 15, 16)
hv	Photon energy	(equ. 17, table 3, figs. 9, 13, 22, 23, 24, 25, 26)
H	Magnetic field	(fig. 11)
I_{ij}	Area of peak *j* from element *i*	(equ. 21)
I	Number of photoelectrons per second in a specific peak	(equ. 22)
I	Intensity (area) of a peak for a surface layer	(equ. 23)
I_0	Intensity (area) of a peak for an infinitely thick sample	(equ. 23)
I_fil	Current over the filament of an electron flood gun	(table 3)
k	Rate constant (forward, backward)	(equs. 5, 7)
k_c	Specific chemical reaction constant (m/s)	(equ. 14)
$\overline{k_c}$	Integrated mean specific chemical reaction constant (m/s)	(equ. 16, table 4)
k_L	Mass transfer coefficient (m/s)	(equ. 11)
k_R	Reactivity (m/s)	(equ. 13)
$k_{R,\,0}$	Initial reactivity (m/s)	(table 4)
$k_{R,\,0\ measured}$	Measured initial reactivity (m/s)	(fig. 18)
$k_{R,\,0\ model}$	Modelled initial reactivity (m/s)	(equ. 33, fig. 18)
K	Overall rate coefficient (1/s)	(equs. 8, 9, 10, 30, fig. 8)
K	Overall chemical reaction constant ($\mathrm{m^3 \cdot kmol^{-1} \cdot s^{-1}}$)	(equ. 32)
KE	Kinetic energy of photoelectrons	(equ. 21)
K_L	Mass transfer rate (1/s)	(equs. 10, 11, fig. 8)
K_R	Kinetic rate (1/s)	(equs. 10, 13, fig. 8)
$L_{ij}(\gamma)$	Angular asymmetry factor for orbital *j* of element *i*	(equ. 21)
m_0	Initial mass of the sample (kg)	(equ. 15)
m_j	Calculated remaining mass of the sample (kg)	(equ. 15)
M	Mass of particles (g)	(equ. 30)
$\overline{M}$	Adsorbate molecular weight	(equ. 29)
n	Reaction order	(equ. 5)
n	Number of electrons	(equ. 18)
n	Integer, order of reflection	(equ. 27)
n_i	Concentration of element *i* within the sampling depth	(equ. 21)
n_i	Number of atoms of the element *i* per sampling depth	(equ. 22)

n_x	Number of atoms of the element x per sampling depth	(equ. 22)
N_S	Shape factor (equal to 1 for spheres) ()	(equs. 11, 13)
$N_{Sh,i}$	Sherwood number ()	(equs. 11, 12)
p	Pressure in a measurement chamber	(table 3)
pCO_2	Partial pressure of carbon dioxide	
P	Equilibrium pressure	(equ. 28)
P_0	Saturation pressure	(equ. 28)
q	Charge on an atom	(equ. 19)
r	Rate of consumption ($\text{mol}\cdot\text{cm}^{-3}\cdot\text{s}^{-1}$)	(equ 31, 32)
r_+	Forward rate, dissolution rate	(equ. 5)
R	Dissolution rate ($\text{mol}\cdot\text{cm}^{-2}\cdot\text{s}^{-1}$)	(equs. 7, 30, 31)
$R_{0,\ 1\text{st}}$	Initial dissolution rate calculated using a first order model ($\text{mol}\cdot\text{cm}^{-2}\cdot\text{s}^{-1}$)	(table 4)
$R_{2\text{nd}}$	Dissolution rate calculated using a second order model ($\text{mol}\cdot\text{cm}^{-2}\cdot\text{s}^{-1}$)	(table 4)
$step$	Energy step size of the measured spectra	(table 3)
S	Sensitivity factor	(equ. 22)
S	Surface area of the reacting particles (cm^2)	(equ. 31)
S_i	Total (BET) surface area	(equ. 29)
SSA	Specific surface area for spherical particles (m^2/kmol)	(equ. 14)
SSA	Specific surface area (cm^2/g)	(equ. 30)
t	Time (s)	(equs. 8, 9, 14, 32)
$T(KE)$	Transmission function of an electron energy analyser	(equ. 21)
v	Electron speed	(fig. 11)
v	Liquid volume (cm^3)	(equ. 31)
V	Liquid volume (m^3)	(equs. 11, 13)
V	Liquid volume (l)	(equ. 30)
V	Potential of the surrounding atoms	(equ. 19)
V_{acc}	Acceleration voltage of the flood gun electrons	(table 3)
V_{fil}	Voltage over the filament of an electron flood gun	(table 3)
W	Weight of adsorbed gas	(equ. 28)
W_m	Weight of a monolayer of adsorbed gas	(equs. 28, 29)
$x_{calcite}$	Calcite/dolomite ratio ()	(equ. 33)
x_{quartz}	Quartz/dolomite ratio ()	(equ. 33)
$y_{sediment}$	$\begin{cases} 1, \text{ if the sample is sedimentary ()} \\ 0, \text{ if the sample is metamorphic ()} \end{cases}$	(equ. 33)
z_i	Mass fraction of particles in size range i ()	(equs. 11, 13)
β	½ of the full width at half maximum	(equs. 24, 25)
ΔE_{b}	Chemical shift between two energy states	(equ. 19)
Δq_i	Change in the charge q on atom i	(equ. 19)
Δq	Charge transfer between anion and cation	(equ. 20)
ΔV_i	Change in the potential of the surrounding atoms	(equ. 19)
ε	Specific stirring power (W/kg)	(equ. 12)

ε	Dielectric function	
θ	Take-off angle with respect to the surface normal	(equs. 21, 23)
θ	Bragg angle	(equ. 27, fig. 15)
λ	Number of atomic layers	(fig. 10)
λ	Wavelength of the X-rays	(equ. 27)
$\lambda(KE)$	Inelastic mean free path	(equs. 21, 23)
ν	Kinematic viscosity of solution (m^2/s)	(equ. 12)
ν	Frequency of a photon	(equ. 17)
ρ	Density of particles (kg/m^3)	(equs. 11, 13)
σ_{ij}	Photoionisation cross-section of peak *j* from element *i*	(equ. 21)
ϕ	Work function of a spectrometer	(equ. 17)
ω	Frequency	
ω_p	Frequency of a bulk plasmon	

Symbols, constants, indices, functions, units and distributions

°	Charge-neutral	(equ. 5)
{}	Concentration	(equ. 5)
>	Surface precursor complex	(equ. 5)
[]	Bulk concentration ($kmol/m^3$)	(equs. 8, 30)
$\int_a^b f(x)dx$	Definite integral	(equs. 16, 26)
*	Convolution	(equ. 26)
∞	Infinity	(equ. 26)
0	Charge-neutral	(equ. 3)
0	Initial	(equs. 15, 30)
0	Infinite thickness	(equ. 23)
0	Position (energy) of a specific peak in a spectrum	(equs. 24, 25)
0	Saturation	(equ. 28)
Al K_α	Characteristic electromagnetic radiation used for XPS	
B	Hydrogen ion, proton	(equ. 14, 32)
c	Speed of light	(fig. 11)
C	BET constant	(equ. 28)
$\frac{d}{dt}$	Time derivative	(equs. 8, 9, 14, 32)
e	$\sum_{n=0}^{\infty}\frac{1}{n!}$	(equs. 9, 23, 25)
eV	Electron volt	(figs. 22, 23, 24, 25, 26)
exp	Natural exponential function, e^x	(equ. 25)
e_0	Electron charge	(equ. 20)
$f(E)$	Voigt function	(equ. 26)
$G(E)$	Gaussian distribution	(equs. 25, 26)
GeV	Giga electron volt	
h	Planck’s constant	(equ. 17)
i	Size range	(equs. 11, 12, 13)
i	Atom *i*	(equ. 19)

i	Element i in a sample	(equs. 21, 22)
Im	Imaginary part of a complex number	
j	Acid addition step ()	(equs. 14, 15, 31, 32)
j	Peak j	(equ. 21)
k	Constant	(equ. 19)
K	Instrumental constant	(equ. 21)
K	Kelvin	
ln	Natural logarithm	(equ. 25)
$L(E)$	Lorentzian distribution	(equs. 24, 26)
M	Molarity	(fig. 3)
Ma	Million years	(table 1)
MeV	Mega electron volt	
$\mathrm{Mg\ K}_{\alpha}$	Characteristic electromagnetic radiation used for XPS	
MΩcm	Mega ohm centimeter	
$\overline{\mathrm{N}}$.	Avogadro's number	(equ. 29)
$R3$	Trigonal space group of dolomite	
$R\bar{3}c$	Trigonal space group of calcite	
Re	Real part of a complex number	
wt%	Weight procent	(table 2)
x	Element x in a sample	(equ. 22)
α_b	Bulk Madelung constant	(equ. 20)
α_s	Surface Madelung constant	(equ. 20)
Δ	Change	(equ. 19)
$\Delta_{s\text{-}o}$	Spin-orbit splitting	
ε_0	Permittivity of vacuum	(equ. 20)
π	Ratio of a circle's circumference to its diameter	(equ. 20)
Σ	Sum	(equs. 11, 13, 22)

Spectroscopic notation for electron orbitals

1s	K	(figs. 9, 24, 25)
2s	L_1	(fig. 9)
$2p_{1/2}$	L_2	(figs. 9, 22, 23, 26)
$2p_{3/2}$	L_3	(figs. 9, 22, 23, 26)
3s	M_1	(fig. 26)

List of publications

This thesis is based on the following four publications, which are cited by their roman numerals in the text.

I. Järvinen, L., Leiro, J.A., Bjondahl, F., Carletti, C., Eklund, O. (2012), XPS and SEM study of calcite bearing rock powders in the case of reactivity measurement with HCl solution, Surface and Interface Analysis 44, 519-528.

II. Carletti, C., Bjondahl, F., De Blasio, C., Ahlbeck, J., Järvinen, L., Westerlund, T. (2013), Modeling limestone reactivity and sizing the dissolution tank in wet flue gas desulfurization scrubbers, Environmental Progress & Sustainable Energy 32, 663-672.

III. Järvinen, L., Leiro, J.A., Heinonen, M. (2014), Core level studies of calcite and dolomite, Surface and Interface Analysis 46, 399-406.

IV. Järvinen, L., Leiro, J.A., Bjondahl, F., Carletti, C., Lundin, T., Gunnelius, K.R., Eklund, O. (2014), Characterisation of dolomites before and after reactivity measurement with HCl solution, Surface and Interface Analysis (DOI: 10.1002/sia.5715).

Contributions

The author was partly responsible for collection and preparation of the samples labelled LJJ. He carried out most of the characterisations done with XPS, SEM, XRD and nitrogen physisorption for papers **I**, **II** and **IV**. For paper **III**, the experiments using synchrotron radiation were conducted in cooperation with the co-authors, whereas the co-authors carried out the conventional XPS measurements. The reactivity experiments were carried out by co-authors. The author is the principal writer of papers **I**, **III** and **IV**, for which he fitted all the XPS and HRXPS spectra. Data analyses and interpretations were mainly done by the author for papers **I** and **IV** (excluding the analysis of nitrogen physisorption data, Rietveld refinement and backward elimination procedure), and in cooperation with the co-authors for paper **III**. Figure 8 in paper **III** was compiled by the author using R statistical software.

In addition, the author has contributed to the following papers that are excluded from this thesis.

Viitanen, V., Leiro, J., Järvinen, L., Eklund, O. (2009), Characterization of different origin limestones by ESCA and SEM/EDX in order to determine their suitability for desulphurization, International Journal of Modern Physics B 23, 1783-1788.

De Blasio, C., Carletti, C., Järvinen, L., Westerlund, T. (2011), Evaluating the reactivity of limestone utilized in Flue Gas Desulfurization. An application of the Danckwerts theory for particles reacting in acidic environments and agitated vessels with Archimedes number less than 40., Computer Aided Chemical Engineering 29, 1225-1229.

Table of Contents

1 Introduction

Limestones have been formed throughout the history of the Earth, since the Archean (>2500 Ma) eon (Trikkel et al., 2012). They appear in different sedimentary environments but carbonate rocks can be found also as metamorphic and magmatic varieties. Limestones have been used by mankind since pre-historical times, for instance in buildings. Their dissolution rates have been studied since at least the 1870s, when Boguski (1876) published the first experimental observations on marble dissolution rates, in order to improve the previous dissolution experiments carried out for zinc. However, very few studies (such as the work of Rauch & White, 1977) have taken into account the geological history of the studied rocks. Therefore, the aim of this thesis has been to combine characterisation of various types of limestones and dolostones with batch dissolution experiments in hydrochloric acid solutions in order to find out which factors influence the dissolution rates.

Overall, studies dealing with dissolution of calcite and dolomite (or limestone and dolostone) are numerous, which is why it is no wonder that several papers and chapters reviewing rates, models, instrumentations, observations etc. have been published (Plummer et al., 1979; Stumm, 1997; Morse & Arvidson, 2002; Morse et al., 2007; Brantley, 2008). For the reasons of this vast interest, a few examples given by Morse & Arvidson (2002) are how fossil fuel-derived CO_2 affects carbonate dissolution, global geochemical cycles, preservation of monuments and buildings, and petroleum reservoir characteristics. In addition, continued release of fossil fuel-derived CO_2 into the atmosphere increases acidity in the oceans (Caldeira & Wickett, 2003), where carbonate formation and dissolution are actual buffering mechanisms. Carbonate dissolution rates at deep ocean floors are studied (Boudreau, 2013), because presence of carbon dioxide can increase solubility of calcium carbonate ($CaCO_3$) by more than a factor of 100 (Geyssant, 2001). Applications of calcium carbonate itself range from using it as filler in paper and plastics industries, to soil improvement in agriculture and building material in construction (Tegethoff et al., 2001).

The main purpose of this thesis, however, was to study limestone dissolution rates for the aim of resolving the varying suitability of raw materials for wet Flue Gas Desulphurisation (FGD). The results can also be applied in the construction industry, where, unlike in wet FGD, slow reactivity of the building material is looked for. One common and still growing (Galuszka, 2012) method to generate heat and electricity is to burn coal in power plants. When coal contains sulphur, sulphur dioxide (SO_2) is formed during combustion through oxidation of sulphur. This SO_2 reacts with water and oxygen to produce sulphuric acid (H_2SO_4), which subsequently contributes to the formation of hazardous acid rains and corrosion of structures. It has also been suggested that excess sulphur dioxide has an influence on global warming (Ward, 2009).

Since the beginning of 1970s, there has been a pursuit to reduce SO_2 emissions (Kiil et al., 1998). One option is to use chemical scrubbing agents, as in limestone-utilising FGD processes (Cheng et al., 2003), that can be divided into dry and wet processes (Karatepe, 2000). Most wet limestone scrubbers appear to be capable of about 90% SO_2 removal, while some advanced wet scrubbers can reach 95% efficiency (Srivastava et al., 2001). Even 99% sulphur dioxide removal has been reported in some wet FGD processes (Kaminski, 2003). In general, wet FGD processes are more efficient in SO_2 removal than dry processes, but it is often tempting to use the latter ones due to their lower capital cost (Liu et al., 2002), especially if the power plant is in operation for only a few more years. More information on the dry method can be found, for example, from the following references (Hu et al., 2011; Davini, 2000; Adnadjevic & Popovic, 2008, Anderson et al., 1995; Zhang et al., 2003; Dam-Johansen & Østergaard, 1991; Chen et al., 2012).

The most common and efficient flue gas desulphurisation method is absorption of SO_2 in a limestone slurry, known as wet scrubbing, which is, according to Kiil et al. (1998), obtained by the overall reaction

$$\mathrm{CaCO_3(s)+SO_2(g)+\frac{1}{2}O_2(g)+2H_2O(l)\rightarrow CaSO_4\cdot 2H_2O(s)+CO_2(g)} \quad (1)$$

where $CaSO_4{\bullet}2H_2O(s)$ stands for gypsum. The dissolution rate of limestone ($CaCO_3$) into the water is crucial on behalf of the overall kinetics and may be the rate controlling step in the SO_2 absorption (Siagi & Mbarawa, 2009). Many investigated full-scale plants for wet flue gas desulphurisation have been reported to produce high quality (high purity, low moisture content and low impurity content) gypsum (Muramatsu et al., 1984; Hansen et al., 2011), which can be used as, for example, a road base (Hua et al., 2010) or raw material for plasterboards and cement (Muramatsu et al., 1984; Lowe & Evans, 1995). In addition to FGD, limestones can also be used for sulphate removal from mine waters through sorption on limestone (Silva et al., 2012). Figure 1 shows a schematic illustration of a full-scale wet FGD packed tower employing co-current gas-slurry contacting (Kiil et al., 1998), which is one way of conducting flue gas desulphurisation.

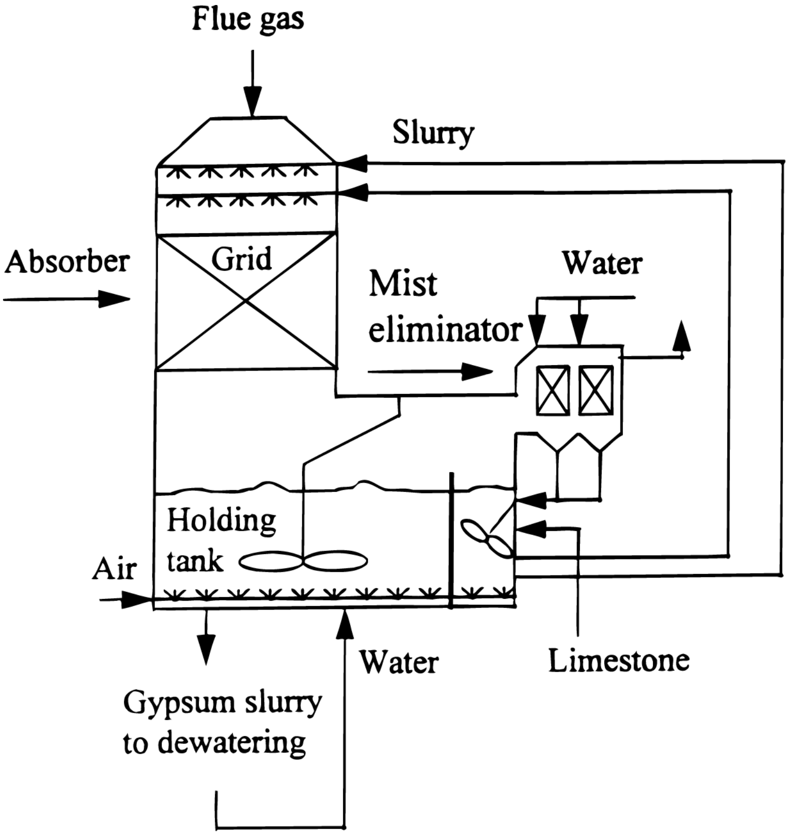

Figure 1. Schematic illustration of a full-scale wet FGD packed tower employing co-current gas-slurry contacting (Muramatsu et al., 1984; Kiil et al., 1998).The whole amount of circulating limestone slurry is distributed evenly from the upper part of the grid, which results as a completely wetted lower section of the absorber that contains a sufficient amount of slurry. Air is injected into the absorber tank for oxidation. Dewatering is performed by centrifugation.

According to Morse & Arvidson (2002), dissolution of a mineral can be divided into a series of different physical and chemical processes that include at least the following steps:

1) diffusion of reactants through solution to the solid surface;
2) adsorption of the reactants on the solid surface;
3) migration of the reactants on the surface to an "active" site (e.g., a dislocation);
4) the chemical reaction between the adsorbed reactant and solid which may involve several intermediate steps where bonds are broken and formed, and hydration of ions occurs;
5) migration of products away from the reaction site;
6) desorption of the products to the solution; and
7) diffusion of products away from the surface to the "bulk" solution.

A primary concept in reaction kinetics is that one of the previous steps, the slowest one, controls the dissolution process (Morse & Arvidson, 2002). As shown in Figure 2 (Brantley, 2008), dissolution of calcite for $pH < 3.5$ is controlled by mass transport of reactants and products through the diffusion boundary layer located between the solid surface and the bulk solution (step 1), whereas for $pH > 3.5$, the rate limiting step is the chemical reactions taking place at the interface (step 4). It has been reported that above *pH* 5.5, dissolution is controlled by mixed kinetics (Sjöberg & Rickard, 1984), which means that both surface reaction rates and hydrodynamic conditions influence rates of dissolution and precipitation from aqueous solutions at mineral-water interfaces (Raines & Dewers, 1997).

Reactants, such as H^+, OH^- and H_2O may form both inner and outersphere complexes when they reach the surface (step 2). In the case of an outer sphere complex, one or more water molecules are placed between the adsorbate and the surface functional group of the adsorbent, whereas for inner sphere complex, loss of hydration water leads to interposition of no water molecules. Migration of the reactants (step 3) and products (step 5) on the surface can be driven by surface concentration gradients, but also by the attempt to find more favourable binding sites that are associated with mineral defects, such as ledge, step or kink sites (Chorover & Brusseau, 2008).

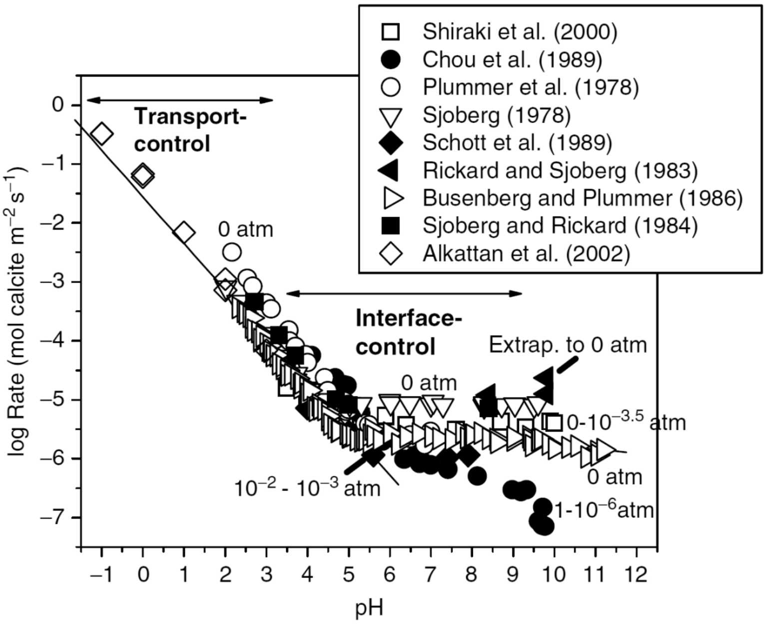

Figure 2. Dissolution rates of calcite as a function of *pH* measured at 298 K and various CO_2 partial pressures. At lower *pH*, the rate is controlled by mass transfer whereas at higher *pH*, the rate is controlled by chemical kinetics. Reproduced from (Brantley, 2008) with kind permission from Springer Science+Business Media.

The rate of limestone dissolution can be estimated by measuring the rate of neutralization of an acid either by allowing the *pH* to change (free drift) and measuring the rate of change of *pH* (Ahlbeck et al., 1995) or by maintaining constant *pH* (*pH*-stat) and measuring the rate of acid addition (Morse, 1974; Siagi & Mbarawa, 2009). The sample has often been in the form of a disc, which has been rotated to reduce or test transport control of dissolution (Boomer et al., 1972; Barton & McConnel, 1979; Rickard & Sjöberg, 1983; Sjöberg & Rickard, 1984). Also, a so called parallel plate method (Nierode & Williams, 1971) and bulk powder experiments (Sjöberg, 1976; Pokrovsky et al., 2000; Pokrovsky & Schott, 2001) have been used. The powder method, which has been used in this thesis (see section 4.2), measures a bulk dissolution rate by changes in solution composition (Lüttge et al., 2013). To relate the rate of consumption of sample material to the surface area of the powder sample (normalisation), both geometric surface area and BET (Brunauer, Emmet, Teller; Brunauer et al., 1938) surface area have been used (Chou et al., 1989; Gautelier et al., 2007). Discussion for application and comparability of the diversely defined surface area terms including the two aforementioned can be found from the literature (Lüttge et al., 1999; Rufe & Hochella Jr., 1999; Gautier et al., 2001; Lüttge, 2005; Fischer & Lüttge, 2007; Noiriel et al., 2009; Rimstidt et al., 2012).

According to the classical paper by Plummer et al. (1978), the three parallel mechanisms that control calcite dissolution are given by

$$\mathrm{CaCO_3 + H^+ \rightleftharpoons Ca^{2+} + HCO_3^-}, \tag{2}$$

$$\mathrm{CaCO_3 + H_2CO_3^0 \rightleftharpoons Ca^{2+} + 2HCO_3^-}, \tag{3}$$

$$\mathrm{CaCO_3 + H_2O \rightleftharpoons Ca^{2+} + HCO_3^- + OH^-}. \tag{4}$$

The backward (precipitation) reaction is driven by the interaction between Ca^{2+} in the bulk fluid and HCO_3^- species on the surface. It is important to keep in mind that during dissolution, also precipitation occurs if the reaction is close to equilibrium. This can have a notable influence on the conclusions (Urosevic et al., 2012).

Further results have shown that equation (3) can be omitted, as carbonate mineral dissolution rates are not proportional to $H_2CO_3^*$ (aq) and depend only weakly on pCO_2 (Pokrovsky et al., 2005). It should be noted that the H_2CO_3 equilibrium depends on *pH*. According to Schott et al. (2009), the dissolution rate for carbonates far from equilibrium can be expressed as

$$r_+ = r_{+,\mathrm{H^+}} + r_{+,\mathrm{H_2O}} = k_\mathrm{H}\left\{>\mathrm{CO_3H^\circ}\right\}^{n_\mathrm{H}} + \mathrm{k}_{\mathrm{H_2O}}\left\{>\mathrm{MeOH_2^+}\right\}^{n_{\mathrm{H_2O}}}, \tag{5}$$

where r_+ is the forward rate, k_i is a rate constant for the species i, {>X} stands for the concentrations of the various rate-controlling surface precursor complexes, Me stands for divalent metal, and n_i represents the reaction order with respect to the subscripted complex. Equation (5) describes calcite and dolomite far from equilibrium dissolution rates with n_H= 2.0, n_{H_2O}= 1.9 (Pokrovsky & Schott, 2001) and n_H= 1.0 (Busenberg & Plummer, 1986), n_{H_2O} = 1.0 (Pokrovsky & Schott, 2002) for dolomite and calcite, respectively.

In studies on the influence of experimental parameters it has been found that the dissolution rate of limestone is enhanced by a decrease of *pH* (Siagi & Mbarawa, 2009; Shih et al., 2000; Rutto et al., 2009; Sun et al., 2010), decrease of particle size (Siagi & Mbarawa, 2009; Hoşten & Gülsün, 2004; Sun et al., 2010) and increase of reaction temperature (Chan & Rochelle, 1982; Siagi & Mbarawa, 2009; Sun et al., 2010). Even though the dissolution experiments are often done with hydrochloric acid to avoid precipitation of gypsum particles, sulphuric acid has also been used (Barton & Vatanatham, 1976; Fellner & Khandl, 1999).

Dolomite ($CaMg(CO_3)_2$), in addition to calcite ($CaCO_3$), is a major constituent of limestones, and should therefore also be taken into account in the quest for suitable raw materials for wet FGD. The dissolution rate of dolomite is reported to be slower than that of calcite (Lerman, 1990; Carletti et al., 2013), which, according to Liu et al. (2005), is due to its more complicated surface reaction controlling mechanism. Dolomite has been reported to dissolve in HCl solution by the reaction (Lund et al., 1973)

$$CaMg(CO_3)_2 + 4H^+ \rightarrow Ca^{2+} + Mg^{2+} + 2CO_2 + 2H_2O. \qquad (6)$$

In their study of dolomites, Busenberg & Plummer (1982) concluded that during a short period of time in the beginning, $CaCO_3$ dissolves faster than $MgCO_3$, and afterwards the dissolution is more stoichiometric. They used an empirical equation describing the dissolution rate *R* as

$$R = k_1 a^n_{H^+} + k_2 a^n_{H_2CO_3^*} + k_3 a^n_{H_2O} - k_4 a_{HCO_3^-} \, , \qquad (7)$$

where k_1, k_2 and k_3 are forward rate constants, k_4 is the backward rate constant, a_i is the activity of the species i, and the reaction order n = 0.5 at temperatures below 45 °C. Chou et al. (1989) used the same equation to describe the forward dissolution rate of dolomite at 25 °C with the exception of n being equal to 0.75. Busenberg and Plummer (1982) found out that the equation of *R* can be simplified to $R_{H^+} = k_1 a^{1/2}_{H^+}$ at 25 °C, near absence of CO_2, far from equilibrium and at *pH* between 0 and 6. According to Pokrovsky et al. (1999) the surface species controlling dolomite dissolution rate in acidic solutions are the protonated carbonates $>CO_3H^o$. Previously obtained dissolution rates for dolomites are shown in Figure 3 (Urosevic et al., 2012).

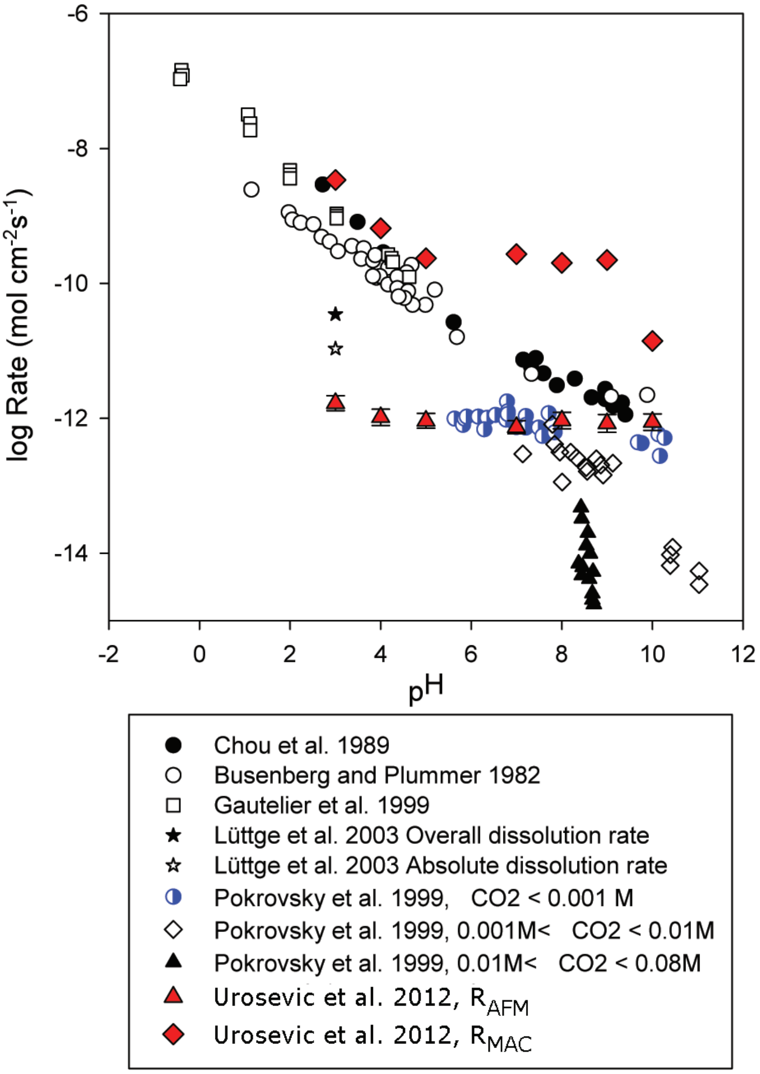

Figure 3. Previously obtained dolomite dissolution rates as a function of *pH* (modified after Urosevic et al., 2012). Macroscopic (bulk) dissolution rates (R_{MAC}) were calculated from the total calcium in the effluent solution. The use of the geometric surface area has led to underestimation of the surface area and overestimation of the rates (Duckworth & Martin, 2004; Urosevic et al., 2012), which explains the high R_{MAC} values. The overall dissolution rate (R_{AFM}) measured by Urosevic et al. (2012) at *pH* 3 is about 25 times lower than that reported by Lüttge et al. (2003). The explanation according to Urosevic et al. (2012) is that Lüttge et al. (2003) measured dissolution rates in deep etch pits most likely originated at dislocations that have high strain. The fact that bulk dissolution rates obtained from powder experiments are higher than the overall dissolution rates obtained by Atomic Force Microscopy (AFM) or Vertical Scanning Interferometry (VSI) is presented to be due to, for example, highly reactive surfaces of the powders and imperfect normalisation of the surface areas of the powders.

One theory which is often used for modelling calcite and dolomite dissolution is the Transition State Theory (TST), which connects the thermodynamics and kinetics of elementary reactions. It was developed in 1935 (Eyring, 1935; Evans & Polanyi, 1935). According to the theory, reactant species form a so called "activated complex" on top of an energy barrier. Further, it assumes that the reaction rate is equal to the product of two terms, the concentration of the activated complex and the frequency with which these complexes cross the energy barrier (Schott et al., 2009). Since then, a series of review articles have been written of the theory itself and its development (Lasaga, 1981; Laidler & King, 1983; Truhlar et al., 1983; Truhlar et al., 1996). TST has been used to, for example, study minerals' dissolution kinetics as a function of Gibbs free energy difference (Lüttge, 2006), although the classical TST model may not be sufficient to describe that relation (Xu et al., 2012).

Another important theory frequently used in dissolution studies is the surface complexation theory (Davis & Kent, 1990; Sposito, 1990). The central concept is that water molecules and dissolved species form chemical bonds with exposed lattice-bound ions at mineral surfaces (Van Cappellen et al., 1993). Supported by the X-ray Photoelectron Spectroscopy (XPS) results of Stipp & Hochella (1991), Van Cappellen et al. (1993) developed a Surface Complexation Model (SCM) that allows an interpretation of the dissolution kinetics of carbonate minerals based on surface speciation. After that, several surface speciation models for calcite and dolomite in aqueous solution has been presented (Pokrovsky et al., 1999; Pokrovsky et al., 2000; Wolthers et al, 2008; Villegas-Jiménez et al., 2009; Pokrovsky et al., 2009). A review of the mechanisms that control dissolution of minerals (calcite and dolomite included) using SCM/TST has been published by Schott et al. (2009). It is, however, emphasised that modelling of chemical reactions/species using SCM or TST is beyond the scope of this thesis.

Since 1992, in situ studies of dissolution in atomic scale have grown increasingly popular. Back then, Hillner et al. (1992) used AFM to observe dissolution and precipitation of calcite. In addition to AFM studies of calcite and dolomite dissolution (Shiraki et al., 2000; Arvidson et al., 2006; Ruiz-Agudo et al., 2009; Ruiz-Agudo et al., 2011; Urosevic et al., 2012), Vertical Scanning Interferometry (VSI) has been successful in the same purpose (Arvidson et al., 2003; Lüttge et al., 2003; Vinson & Lüttge, 2005; Arvidson et al., 2006; Vinson et al., 2007). VSI studies have been used to formulate a dissolution stepwave model (Lasaga & Lüttge, 2001), that describes dissolution in terms of moving and coalescing "stepwaves" wiping away one atomic layer at a time. Later, Urosevic et al., (2012) demonstrated that (overall) dolomite dissolution rate is controlled by the removal of dolomite layers by spreading and coalescence of shallow etch pits rather than by step retreat from deep pits nucleated at high energy points (dislocations). A newer emerging trend in dissolution studies could be the development of a stochastic approach that includes variance as a key parameter (Fischer et al., 2012; Lüttge et al., 2013).

2 Aim of the research

The aim of this work was to gain a better understanding of the varying chemical reactivities and dissolution rates of different limestones and dolostones. Information of the dissolution process needs to be supported by information of the dissolving materials' characteristics, which is why the samples were characterised, their chemical reactivities and dissolution rates were obtained, and the bonding environments of calcite and dolomite were studied via core-level photoemission.

2.1 Methodological premises

At Åbo Akademi University, Ahlbeck et al. (1995) studied variations in reactivities of limestones. In the present study, Ahlbeck's data has been expanded with a larger group of samples in order to obtain a more comprehensive general view of how much the reactivities vary among different limestones and dolostones (**I**, **II**, **IV**). The experiments were carried out at Process Design and Systems Engineering Laboratory at Åbo Akademi University using stepwise titration with hydrochloric acid. Using two different mathematical models and *pH* regions, either initial reactivities or integrated mean specific chemical reaction constants were obtained for comparison of the samples' reactivities. The terms "initial reactivity" and "integrated mean specific chemical reaction constant" are explained in the section 4.2. Also, dissolution rates were calculated from the reactivity data for easier comparison with literature values.

The reactivities were accompanied by characterisation (**I**, **II**, **IV**) done with the purpose of elucidating which characteristics have an influence on the dissolution rates. An emphasis was put on chemical and morphological changes taking place at the particle surfaces via X-ray Photoelectron Spectroscopy (XPS) and Scanning Electron Microscopy (SEM). Supporting chemical information was obtained with X-Ray Fluorescence (XRF) measurements of the samples, and Inductively Coupled Plasma-Mass Spectrometry (ICP-MS) and Inductively Coupled Plasma-Optical Emission Spectrometry (ICP-OES) measurements of the solutions used in the reactivity experiments. Information on mineral (modal) compositions and their occurrence was provided by X-Ray Diffraction (XRD), Energy Dispersive X-ray analysis (EDX) and studying thin sections with a petrographic microscope. BET surface areas were determined from nitrogen physisorption data.

Finally, core-level photoemission studies (**III**) aimed at gaining new information on the bonding environments in calcite and dolomite. More accurate binding energies of electrons and binding energy shifts may help to create more accurate theoretical models of calcite and dolomite dissolution.

3 Materials

3.1 Limestone and dolostone

Limestones mainly consist of the rhombohedral mineral calcite ($CaCO_3$), which is one of the most common minerals in the Earth's crust (Geyssant, 2001). One less common polymorph is orthorhombic aragonite, and even more infrequent is the unstable vaterite, which has a hexagonal crystal structure. In nature, they appear in a multitude of sedimentary environments, but also magmatic deposits occur, in which case the calcium carbonate rock is called carbonatite (Geyssant, 2001). One example is Halpanen in South-Eastern Finland (Puustinen & Karhu, 1999), that formed during the post-orogenic uplift stage of the Svecofennian orogeny approximately 1792 million years ago (Rukhlov & Bell, 2010). Under metamorphosis, a limestone turns into marble with simultaneous grain size increase. A specimen in this thesis is called limestone, if more than half of it is composed of calcium carbonate (according to XPS measurements). For smaller proportions, the term calcareous is used. More detailed classifications for various types of limestones are given elsewhere (Geyssant, 2001; Wright, 1990).

Calcite (space group $R\bar{3}c$) has a rhombohedral crystal structure. It consists of alternating layers of calcium (Ca^{2+}) and carbonate (CO_3^{2-}) ions that are perpendicular to the crystallographic c-axis. Each calcium ion is coordinated by six oxygen atoms. The coplanar vectors a and b of the calcite unit cell have the same length of 0.499 nm and an angle of 120° between them, whereas the perpendicular c axis is 1.706 nm long (Rode et al., 2009).

Figure 4 shows the hexagonal unit cell of calcite and the $(10\bar{1}4)$ cleavage plane, which is the most frequently observed surface of calcite. There are excellent cleavage properties along it because no covalent C-O bonds and the least amount of ionic Ca-O bonds are broken (Skinner et al., 1994; Reeder, 1983). In the figure, the missing (above plane) oxygen atoms are shown. On the $(10\bar{1}4)$ surface, each Ca^{2+} ion is coordinated to 5 nearest-neighbour oxygen atoms instead of 6 in the bulk (Cheng et al., 1998).

Dolostones mainly consist of the mineral dolomite ($CaMg(CO_3)_2$), which has a wide occurrence in sedimentary strata, but they may also be recrystallised by metamorphism (Mason & Berry, 1968; Trikkel et al., 2012). Dolomites experiencing metamorphism become coarser grained, primary sedimentary structures disappear and Ca-Mg-silicates can be formed due to reactions with SiO_2-rich impurities. Usually dolomites are formed from already existing calcites in a process called dolomitisation. In the process, calcite is infiltrated

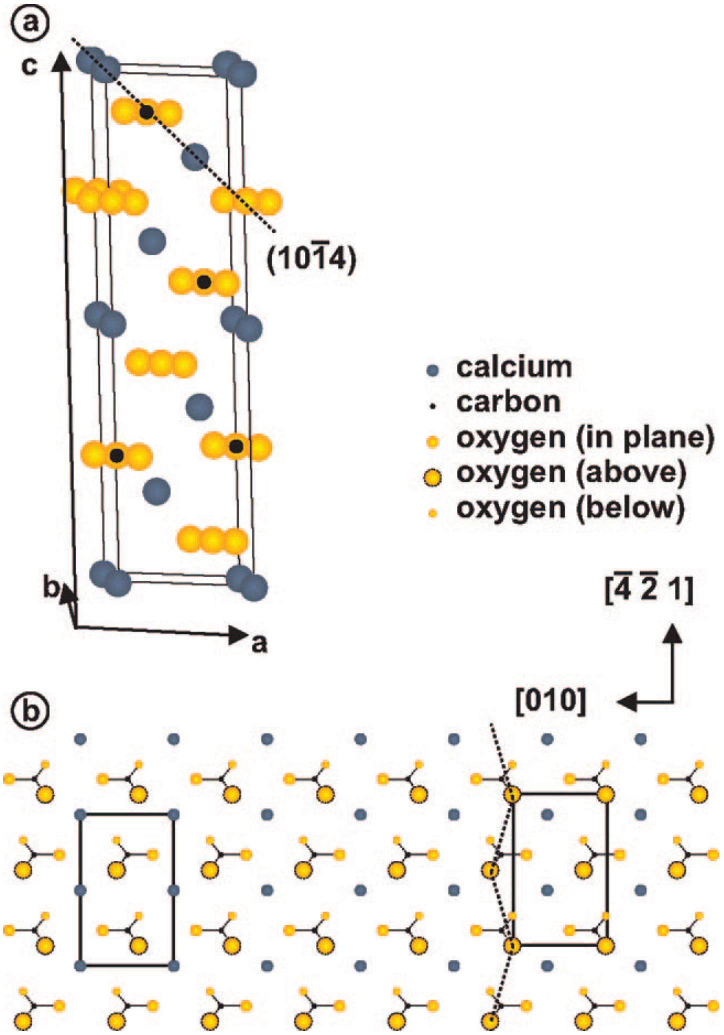

Figure 4. (a) Hexagonal calcite unit cell with the cleavage plane (10$\bar{1}$4) indicated by a dashed line. (b) Truncated bulk surface structure of the (10$\bar{1}$4) cleavage plane. The two different unit cells indicated in the figure consider calcium ions (left) or the protruding oxygen atoms (right) (Rode et al., 2009).

by magnesium rich solutions, which can form in variable environments. Higher Mg/Ca ratio in the infiltrating solution leads to a more stoichiometric composition of the dolomite (Kaczmarek & Sibley, 2011). The dolomitisation process needs efficient hydrological circulation, and usually not all of the calcite is converted to dolomite. This is why calcite and dolomite (limestone and dolostone) are often found in the same geological environment. Dolomite can also precipitate straight from solution into the pore spaces of the sediments (Machel, 2005). A specimen in this thesis is called dolostone, if more than half of it is composed of dolomite.

Dolomite ($CaMg(CO_3)_2$), as well as calcite, is also a rhombohedral carbonate mineral with slightly lower symmetry (space group *R*3). The difference to the calcite crystal structure is that every other Ca^{2+} layer, which are perpendicular to the crystallographic c-axis, is replaced by magnesium (Mg^{2+}) ions (Wenk & Bulakh, 2008; Mason & Berry, 1968; Titiloye et al., 1998). This, however, is only an ideal case. In practice, Mg-layers can accommodate Ca^{2+}-ions and vice versa so the Ca/Mg-ratio can vary in dolomites. In other words, calcium and magnesium can substitute each other in the mineral lattice.The end members of this solid solution series are called calcite ($CaCO_3$) and magnesite ($MgCO_3$). The common carbonate solid solution series are shown by the carbonate tetrahedron in Figure 5. The lattice parameters of a = b = 0.488 nm and c = 1.629 nm have been published (Hossain et al., 2011). The $(10\bar{1}4)$ cleavage plane of a perfect dolomite is shown in Figure 6.

Calcite is a strong insulator, which means that the forbidden region between valence and conduction bands is large. Experimental determination of its indirect electronic band gap yielded a result of 6.0 eV (Baer & Blanchard, 1993). Calculated values of 5.11 eV (Akiyama et al., 2011) and 5.023 eV (Brik, 2011) have been obtained. Dolomite is also an insulator. The indirect electronic band gap of dolomite is 5.0 eV (Hossain et al., 2011).

3.2 Samples included in this thesis

A wide range of limestones and dolostones with varying characteristics was central for the aims of this study. The used samples were of sedimentary, magmatic or metamorphic origin. They have been collected from countries around the Baltic Sea and from China. Information concerning the geological background of the samples is given in Table 1. A consistency with papers I-IV is maintained by using the same codes. In paper I, the limestones were labelled with an L as the final letter (LJJ-01L, LJJ-04L, LJJ-05L, LJJ-09L), whereas the ending C stood for a calcareous rock (LJJ-06C – 08C). A sample was classified as a calcareous rock if the combined atomic concentration of Ca, C and O (approximately three times the concentration of Ca) measured with X-ray Photoelectron Spectroscopy was less than 50%. All other samples end with the letter C, which originally stood for a carbonate. Chemical compositions of the samples measured with X-ray Fluorescence are given in Table 2. Large amounts of impurities are found in the calcareous rocks. For limestones, CaO content varies between 50 and 55 wt%.

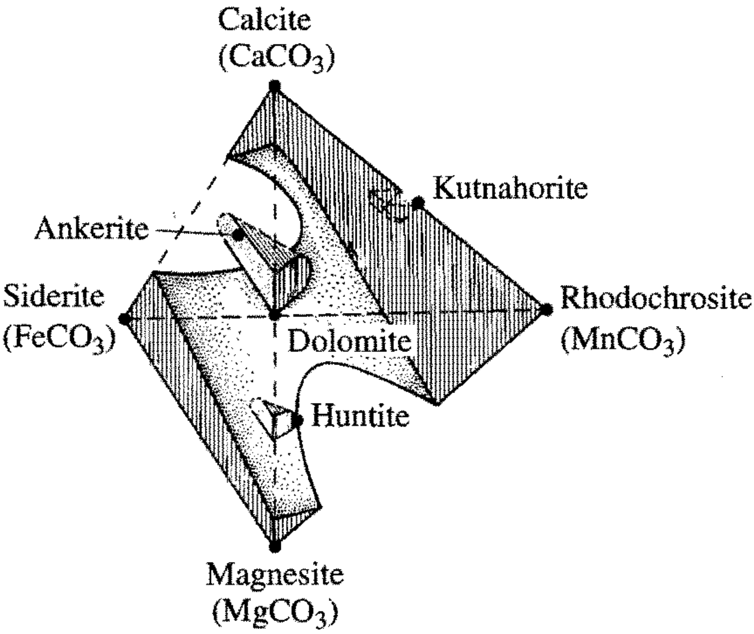

Figure 5. Variable chemical compositions of rhombohedral carbonates. Most of the observed chemical compositions, represented by the shaded regions, are close to the end-members. The void spaces represent unobserved compositions. Reproduced from (Wenk & Bulakh, 2008) with permission from Cambridge University Press.

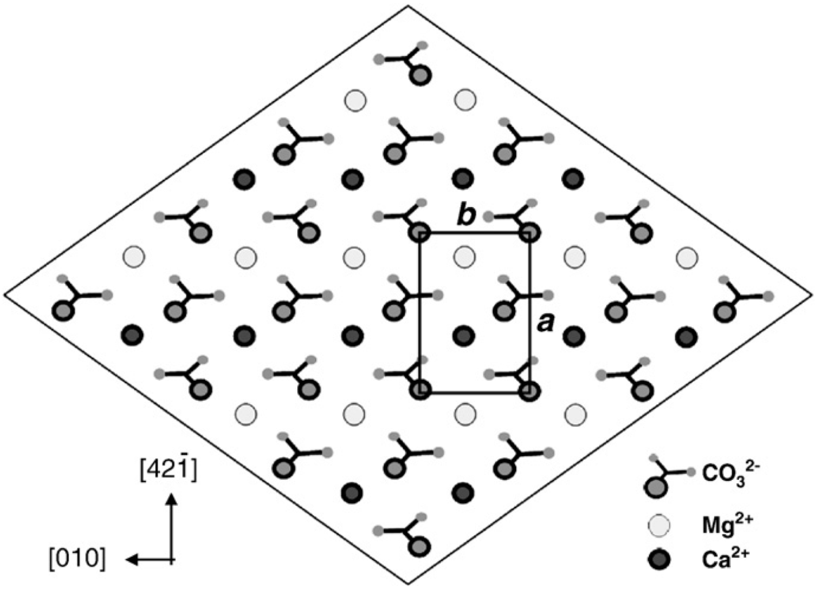

Figure 6. The (10$\bar{1}$4) cleavage plane of a stoichiometric dolomite (Pina et al., 2010).

Table 1. Geological background of the samples. (**I**, **II**, **III**, **IV**)

Sample	Type	Provenience	Age	Stratigraphy remarks
JJ-01C	Metamorphic dolostone	Loukolampi, Ankele mine, Finland	Proterozoic (1900 – 2000 Ma)	
JJ-02C	Metamorphic dolostone	Loukolampi, Ankele mine, Finland	Proterozoic (1900 – 2000 Ma)	
JJ-03C	Metamorphic dolostone	Reetinniemi, Finland	Proterozoic (1900 – 2000 Ma)	
JK-01C	Metamorphic dolostone	Tornio, Kalkkimaa mine, Finland	Early Proterozoic (2050 Ma)[1]	
JK-02C	Metamorphic dolostone	Tornio, Kalkkimaa mine, Finland	Early Proterozoic (2050 Ma)[1]	
JK-03C	Metamorphic dolostone	Virtasalmi, Ankele mine, Finland	Early Proterozoic (1900 – 2000 Ma)	
LJJ-01L	Magmatic limestone	Halpanen, South-Eastern Finland	Precambrian (1792 Ma)[2]	
LJJ-04L	Sedimentary limestone	Daijiagou, Tongzi, Guizhou (close to Guiyang), China	Silurian, Llandovery (428 - 444 Ma)	Hanchiatien Fm
LJJ-05L	Sedimentary limestone	Zhuzhai section, Yushan, Jianxi (close to Nanchang), China	Upper Ordovician (444 – 461 Ma)	Xiazhen Fm
LJJ-06C	Sedimentary calcareous rock	Wangjawan River section, Yichang, Hubei (close to Wuhan), China	Upper Ordovician (444 – 461 Ma)	Linshiang Fm
LJJ-07C	Sedimentary calcareous rock	Daijiagou, Tongzi, Guizhou (close to Guiyang), China	Silurian, Llandovery (428 – 444 Ma)	
LJJ-08C	Sedimentary calcareous rock	Wulongguan section, Yichang, Hubei (close to Wuhan), China	Silurian (416 – 444 Ma)	Lojoping Fm
LJJ-09L	Metamorphic limestone	Parainen, South-Western Finland	Paleoproterozoic (1900 Ma)[3]	
LJJ-15C	Sedimentary limestone	Wolica, Poland	Jurassic (150 Ma)[3]	
LJJ-21C	Sedimentary limestone	Gotland, Sweden	Silurian (430 Ma)[3]	
LJJ-26C	Metamorphic limestone	Kolari, Finland	Precambrian (2000-2200 Ma)	
LJJ-27C	Sedimentary limestone	Röngu, Estonia	Devonian (359-416 Ma)	
LJJ-28C	Sedimentary dolostone	Otepää, Estonia	Devonian (359 – 416 Ma)	
LJJ-29C	Sedimentary dolostone	Kose, Estonia	Upper ordivician (443 – 460 Ma)	
LJJ-30C	Sedimentary limestone	Tallin-Tartu, Estonia	Silurian (416-444 Ma)	

[1] Wampler & Kulp (1962)
[2] Rukhlov & Bell (2010)
[3] Nordkalk Corp. (2008)

Table 2. Chemical compositions (wt%) of the prepared rock powders (see section 4.1) measured with X-Ray Fluorescence. CaO/MgO ratio is shown for dolostones. (**I**, **II**, **IV**, unpublished data).

	Limestones								**Carbonatite**
	Sedimentary						**Metamorphic**		**Magmatic**
	LJJ-04L	LJJ-05L	LJJ-15C	LJJ-21C	LJJ-27C	LJJ-30C	LJJ-09L	LJJ-26C	LJJ-01L
CaO	50.1	51.7	54.4	54.6	53	52.6	54.5	51.5	51.8
SiO_2	5.2	4.6	1.1	0.22	2.6	0.27	0.5	4.5	0.38
TiO_2	0.04	0.02	<0.01	<0.01	0.03	<0.01	<0.01	0.02	<0.01
Al_2O_3	1.1	0.46	<0.01	0.1	0.54	0.05	0.13	0.28	<0.01
Fe_2O_3	1	0.24	0.13	0.06	0.42	0.1	0.16	1.1	0.66
MgO	0.9	0.82	0.44	0.43	0.52	2.5	0.59	1.1	0.4
K_2O	0.24	0.11	0.01	0.02	0.26	0.02	0.03	0.19	0.01
Na_2O	0.1	0.02	0.01	0.02	0.02	0.03	0.01	0.01	0.02
MnO	0.31	0.02	0.02	0.01	0.04	0.01	0.01	0.08	0.14
P_2O_5	0.06	0.01	0.01	0.01	0.03	<0.01	0.01	0.02	5.1
SrO	-	-	-	-	-	-	-	-	-
CO_2	40.8	41.8	43.6	44.6	42.3	44.3	43.8	40.5	38.4
Total	99.9	99.8	99.8	100.1	99.8	99.9	99.7	99.8	97.04

	Dolostones								**Calcareous rocks**		
	Sedimentary		**Metamorphic**						**Sedimentary**		
	LJJ-28C	LJJ-29C	JJ-01C	JJ-02C	JJ-03C	JK-01C	JK-02C	JK-03C	LJJ-06C	LJJ-07C	LJJ-08C
CaO	30.8	30.8	34.6	35.2	30	28.4	32.2	31.3	31.1	32.1	47.9
SiO_2	1.3	1.5	5.7	1.8	4.5	6	1.6	14.4	26.6	28.7	8
TiO_2	0.01	0.02	<0.01	<0.01	0.05	0.12	0.02	0.03	0.29	0.3	0.08
Al_2O_3	0.2	0.29	<0.01	0.06	1.2	1.8	0.26	1.4	6.4	5.9	1.9
Fe_2O_3	0.35	0.39	0.07	0.1	0.99	2.1	0.63	0.55	4.6	2.4	1.1
MgO	19.9	19.7	17.4	17.3	19.4	17.8	19	15.8	1.6	1	0.77
K_2O	0.08	0.11	0.01	<0.01	0.14	0.78	0.13	0.19	1.7	1.5	0.46
Na_2O	<0.01	<0.01	<0.01	<0.01	0.05	0.01	<0.01	0.31	0.31	0.7	0.15
MnO	0.1	0.07	0.01	0.01	0.08	0.06	0.1	0.02	0.16	0.11	0.21
P_2O_5	<0.01	0.01	0.07	0.11	0.05	0.04	0.04	0.07	0.04	0.06	0.04
SrO	0.01	0.01	0.01	0.01	0.01	0.01	0.01	0.01	-	-	-
CO_2	47.2	46.9	42	45.4	43.3	42.8	46	35.7	25.6	27	39.2
Total	100	99.8	99.9	100	99.8	99.9	100	99.8	99.9	99.8	99.8
CaO/MgO	1.55	1.56	1.99	2.03	1.55	1.6	1.69	1.98			

4 Experimental

4.1 Sampling and sample preparation

Rock samples were acquired from mines, corporations and colleagues. Arto Peltola, Jani Jäsberg and Jaakko Kara (University of Turku) prepared the thin sections. The mineralogy was studied under a petrographic microscope. The powders were prepared by crushing the stones with a jaw crusher and subsequently grinding to smaller particles with a vibratory disc mill. Using sieves, a suitable amount of material for dissolution and characterisation experiments was gathered to three size fractions of 63 – 106 µm, 106 – 150 µm and 150 – 250 µm. Each sample fraction was first rinsed 4 – 6 times with tap water (*pH* ~8.0) and finally twice with distilled water to remove fine particles. The resulting samples were dried under ambient laboratory conditions.

4.2 Reactivity experiments (I, II, IV)

In order to estimate suitability of carbonate rocks for wet flue gas desulphurisation, their dissolution reactions were studied at the Laboratory of Process Design and Systems Engineering at Åbo Akademi University. In the desulphurisation process, SO_2 is first absorbed into the water. Hydrolysis decreases *pH* by forming hydrogen ions and sulphite ions, which are in turn oxidized into sulphate ions. An acid is often used instead of SO_2 to eliminate the gas absorption step in the process, and simplify the experimental setup. Adding sulphuric acid leads to the formation of the same reaction products. The sulphate ions react with dissolved calcium ions and form calcium sulphate while the hydrogen ions react with the carbonate ions to form water and carbon dioxide. Small particles can be formed because calcium sulphate ($CaSO_4$) has a solubility of 0.209 g $CaSO_4$ per 100 g H_2O at 30 ºC (Polig et al., 2008). The measurement of the particle size distribution of the limestone particles is central to the used method for calculation of the reactivity of a sample, which is why formation of new particles should be avoided. Therefore, sulphuric acid is replaced by another strong acid, hydrochloric acid, in order to avoid the formation of calcium sulphate particles. Precipitation of $CaCl_2$ is far less probable than precipitation of $CaSO_4$, because the former has a solubility of 102 g $CaCl_2$ per 100 g of H_2O at 30 ºC (Polig et al., 2008).

Figure 7 depicts the experimental setup for reactivity experiments in schematic form. About 1 – 2 g of ground particles and 500 ml of deionised water (18.2 MΩcm) were combined in a beaker (reactor) to create a suspension with a suitable particle concentration for the measurement

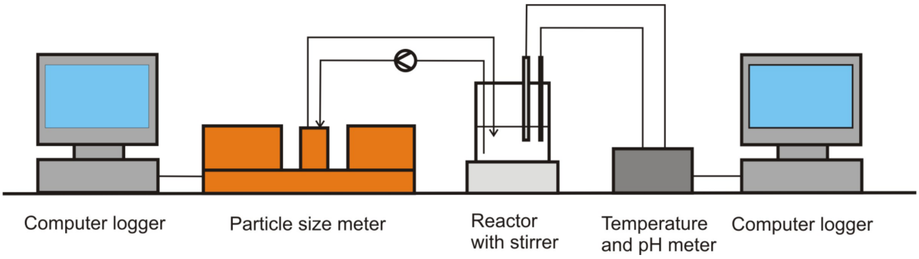

Figure 7. A schematic illustration of the experimental setup for the measurement of initial reactivities.

of particle size distributions using laser diffraction technique. A magnetic stirrer was used to stir the suspension at 450 – 850 rpm to ensure complete suspension of the particles. Ambient temperature of 25 °C was used. Hydrochloric acid (0.1 M HCl) was added in 10 steps (10 ml per step). The size distribution of the particles was measured before each step and after the final step, while *pH* was measured continuously. The *pH* range of 3.5 to 4 was used to evaluate the rate of reaction. A method developed by Ahlbeck et al. (1993, 1995) and later described in paper **I** was used to calculate the reactivity of the samples from the rate of change of *pH* and particle size distribution. The reactivity was normalised to geometric surface area of the assumedly spherical particles.

The rate of change in hydrogen ion concentration was modelled with a first order rate equation

$$-\frac{\mathrm{d}\left[\mathrm{H}^{+}\right]}{\mathrm{d}t}=K\left[\mathrm{H}^{+}\right], \tag{8}$$

where $[\mathrm{H}^+]$ is the bulk concentration of hydrogen ions (kmol/m^3) and K is the overall rate coefficient (1/s). The overall rate coefficient was calculated from *pH* data using

$$K=\frac{1}{\log e}\frac{\mathrm{d}pH}{\mathrm{d}t}\ . \tag{9}$$

Equation (9) follows from equation (8) by integration. Ahlbeck et al. (1995) split the overall rate into two parts, one depending on the rate of the surface reaction and one depending on the mass transfer of hydrogen ions through the diffusion boundary layer of molecules and ions that is surrounding the dissolving particle, using

$$\frac{1}{K}=\frac{1}{K_R}+\frac{1}{K_L}\ . \tag{10}$$

The mass transfer rate was estimated from the specific stirring power and the particle size distribution using

$$K_L = k_L \frac{A}{V} = D_{\mathrm{H}^+} c \frac{N_S 6}{\rho} \sum_{i=1}^{i_{\max}} N_{Sh,i} \frac{z_i}{d_i^2} , \qquad (11)$$

where k_L is the mass transfer coefficient (m/s), A is the surface area of the assumedly spherical particles (m^2), V is the liquid volume (m^3), D_{H^+} is the diffusivity of the hydrogen ion in water (m^2/s), c is the mass concentration of particles in the suspension (kg/m^3), N_S is a shape factor which is assumed to be 1 (for spherical particles), ρ is the particle density (kg/m^3) and z_i is the mass fraction of particles of average size d_i (m) in size range i. The Sherwood number $N_{Sh,i}$ for each particle size was estimated with

$$N_{Sh,i} = 2 + 0.13 \left(\frac{d_i}{D_{\mathrm{H}^+}} \right) \left(\frac{\nu}{D_{\mathrm{H}^+}} \right)^{-\frac{2}{3}} (\varepsilon \nu)^{\frac{1}{4}} , \qquad (12)$$

where ν is the kinematic viscosity of the solution (m^2/s) and ε is the specific stirring power used (W/kg). The specific stirring power was estimated from the power used by the stirrer at different speeds. The kinetic rate (K_R) is calculated from the measured overall rate and the estimated mass transfer rate. The reactivity k_R (m/s) was estimated from the kinetic rate using

$$K_R = k_R \frac{A}{V} = k_R c \frac{N_S 6}{\rho} \sum_{i=1}^{i_{\max}} \frac{z_i}{d_i} . \qquad (13)$$

The result is reported as reactivity which is independent of both the surface area of the particles and the particle size distribution (see equation 13). As the experiments proceeded, the reactivities decreased exponentially while the samples were consumed. For each sample, a least squares method was used to fit an exponential curve to the reactivity data points from each acid addition step. The fitted exponential curves were extrapolated backwards to obtain estimates of the reactivities at the very beginning of the experiments. These estimates are called initial reactivities ($k_{R,0}$), and they can be used for comparison of the samples. During the dissolution experiments, the conditions in the suspension remained far from equilibrium. Conversions of approximately 60% were reached.

After each reactivity experiment, the beaker was rinsed with distilled water in order to release any particles attached to the walls of the beaker. The solid remainder, which was used in the “after experiment” XPS and SEM analyses, was vacuum-filtered with filter paper and dried in an oven at 110 °C. The filter paper with filtrate was cooled in a desiccator.

The reactivity was not always possible to calculate since the reactions were relatively fast and the overall rates became limited by the mass transfer rates. Examples of where the overall rate is limited by mass transfer rate and kinetic rate are shown in Figure 8. For sample LJJ-07C (a calcareous rock, upper panel), the measured overall rate coefficient follows the data points of K_R (kinetic rate coefficient), which means that the overall rate is controlled (limited) by the kinetic rate. In the case of LJJ-09L (a metamorphic limestone, lower panel), the mass transfer rate coefficient (K_L) is lower than K_R (i.e. overall rate limiting) and following the overall rate coefficient calculated from the rate of change of *pH*. The fact that K_L is lower than K_R means that the mass transfer resistance through the diffusion boundary layer ($1/K_L$) is larger than the resistance for chemical reaction at the surfaces of the particles ($1/K_R$). Hence, only mass transfer coefficients can be obtained, and the chemical reactivity (k_R) cannot be estimated under these experimental conditions. Mass transfer limitation prevailed among all the limestone samples for the given experimental setup. Increasing the stirring speed did not help.

For paper **II**, the experimental conditions and the dissolution modelling were modified so that the used *pH* region was 4–5. This should lead to chemical kinetics controlled dissolution. Also, the dissolution model was based on a reaction that was of second instead of first order, and the model assumes that only $CaCO_3$ is reacting. The specific chemical reaction constants k_c (m/s) were calculated from the equation

$$-\left[\frac{\mathrm{d}C_{\mathrm{CaCO_3}}}{\mathrm{d}t}\right]_j = k_{c,j}\cdot SSA_j\cdot C_{\mathrm{B}}\cdot C_{\mathrm{CaCO_3}}\,, \tag{14}$$

where $C_{\mathrm{CaCO_3}}$ is the calcium carbonate concentration (kmol/m^3) estimated from the remaining mass fraction (*fR*) of calcium carbonate, *t* is time (s), the subscript *j* stands for the *j*th acid addition step, *SSA* is the specific surface area calculated from particle size distribution for assumedly spherical particles (m^2/kmol) and C_{B} is the concentration of H^+ (kmol/m^3) obtained from the rate of change of *pH*. The remaining mass fraction (fR_j) was calculated according to

$$fR_j = \frac{m_j}{m_0}\,, \tag{15}$$

where m_j is the calculated remaining sample mass (kg) for every acid addition step *j* according to stoichiometry and m_0 is the initial mass of the sample. Integrated means for the exponential fittings of the specific chemical reaction constants were estimated according to

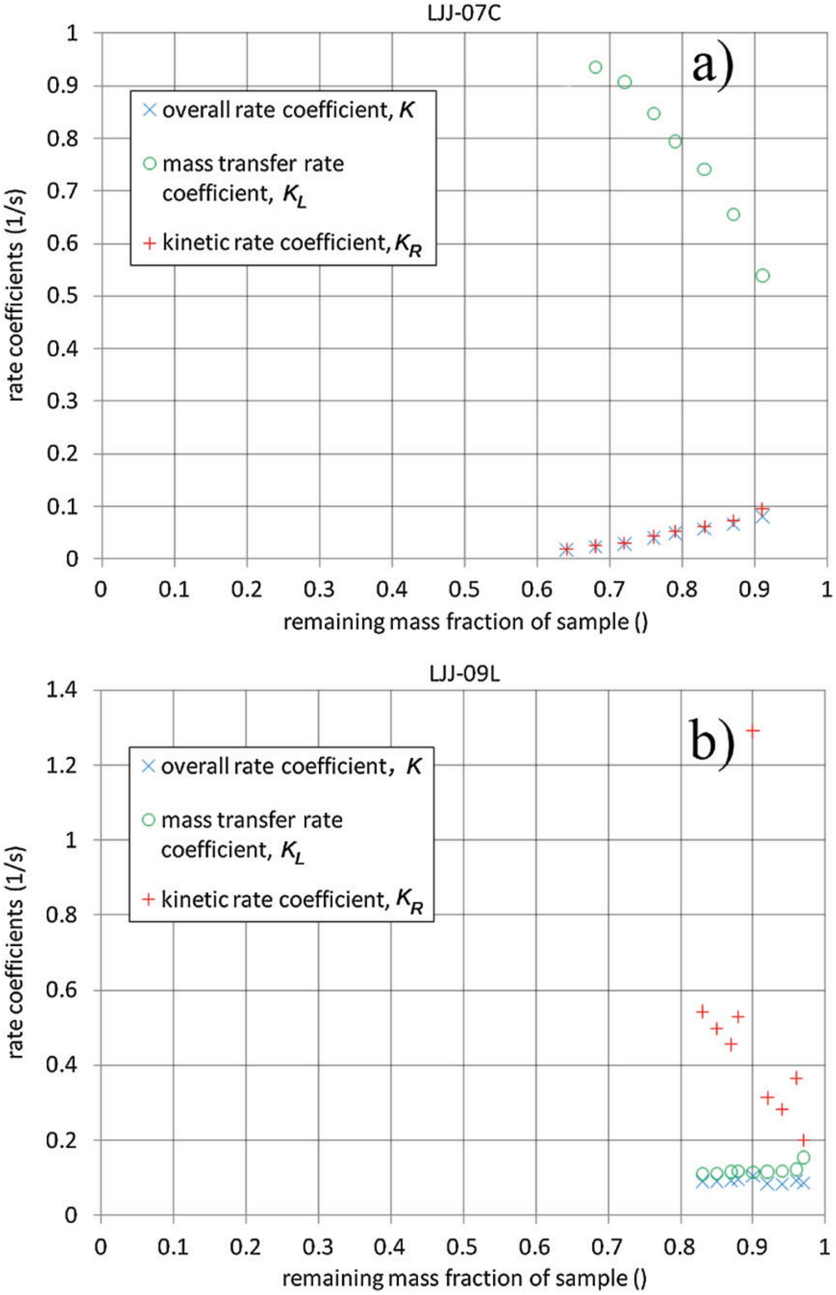

Figure 8. The dissolution rate can be limited by the kinetic rate (a) or by the mass transfer rate of H^+ ions (b). In part (a), the overall rate coefficients closely follow the kinetic rate coefficients, which are lower than mass transfer rate coefficients. Therefore the dissolution rate is limited by the surface reaction kinetics. In part (b) the roles of mass transfer and chemical kinetics are reversed. (**I**)

$$\overline{k_c} = \frac{\int_{inerts}^{1} A \cdot e^{B \cdot (fR)^C} \mathrm{d}(fR)}{\int_{inerts}^{1} \mathrm{d}(fR)} , \tag{16}$$

where the integration goes from the fraction of inerts (other than calcite) to 1, and A, B and C are fitting parameters obtained from an exponential regression.

4.3 Characterisation

The following methods have been used for characterisation of the samples:

1. X-ray Photoelectron Spectroscopy (XPS) has been used to measure the chemical compositions of the surfaces before and after reactivity experiments (**I**, **IV**). Also, bonding environments have been analysed (**III**).

2. Synchrotron based high resolution (HRXPS) measurements (**III**) were used to support XPS studies of bonding environments.

3. Scanning Electron Microscopy (SEM) was used to study surface topography of the particles before and after reactivity experiments (**I**, **II**, **IV**). Energy Dispersive X-ray analysis (EDX) was carried out to study the mineral (modal) compositions of the thin sections (**IV**).

4. X-Ray Diffraction (XRD) was used to identify the mineral phases of the samples (**I**, **III**, **IV**). With the help of Rietveld Refinement, the proportions of the phases were estimated (**IV**).

5. The chemical compositions of bulk powder samples were acquired using X-Ray Fluorescence (XRF) (**I**, **II**, **IV**).

6. Inductively Coupled Plasma-Optical Emission Spectrometry (ICP-OES) and Inductively Coupled Plasma-Mass Spectrometry (ICP-MS) were used to measure elemental concentrations in the solutions after reactivity experiments (**IV**).

7. The surface areas of the samples were obtained using nitrogen physisorption and BET plots (**IV**).

4.3.1 X-ray Photoelectron Spectroscopy (XPS)

X-ray Photoelectron Spectroscopy (XPS), or ESCA (Electron Spectroscopy for Chemical Analysis) was in large part developed by Kai Siegbahn and his research group during the 1950s and 1960s (Siegbahn et al., 1967). It is based on the photoelectric effect, in which a surface of a sample is irradiated by X-rays. As a result, photon energy can be transferred to atomic core orbital electrons that are ejected if the photon energy is sufficiently high. This photoemission process is shown in Figure 9. The following discussion is intended to cover only core level XPS. Valence spectra are outside the scope of this thesis.

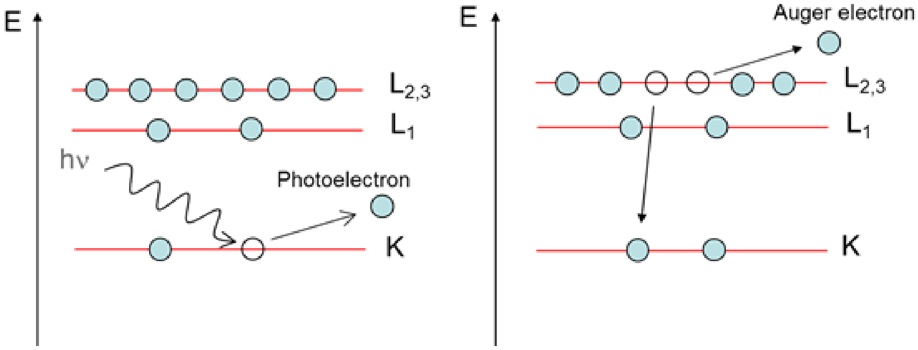

Figure 9. Emission of a photoelectron takes place when a core level electron absorbs energy from a photon and is subsequently ejected from the matter (left). Empty states can be filled by electrons from higher energy levels. Such a process may lead to emission of an Auger electron through, for example, a normal Auger decay (right).

When the photon energy is sufficiently high, the number of emitted photoelectrons will be determined by the intensity of the irradiation, and the inelastic mean free path of the photoelectrons, which is a function of kinetic energy (see section 4.3.1.2 Surface sensitivity). At different photon energies the inelastic mean free path specifies the relative numbers of the electrons originating from different depths, while the intensity of the irradiation contributes to the total number of photoelectrons. The binding energy tells how tightly electrons are bound to their orbitals, and therefore also how much photon energy is needed for photoemission. This is given by

$$E_\mathrm{b} = \mathrm{h}\nu - E_\mathrm{k} - \phi, \qquad (17)$$

where E_b is the binding energy of the core orbital from which the photoelectron is emitted, hν is the energy of an X-ray photon, ν is the frequency of the photon, h is Planck's constant, E_k is the kinetic energy of the emitted photoelectron and ϕ, which is called the work function of the spectrometer used for the realisation of the XPS experiment, is the amount of energy needed to move the photoelectron from the material into vacuum.

In an XPS experiment, Mg K_α (hν = 1253.6 eV) and Al K_α (hν = 1486.6 eV) excitation sources are commonly used. Unlike the latter, the former radiation is usually non-monochromatic. Therefore, X-ray satellite peaks can be seen in the spectra. Binding energy is defined as the energy difference between initial and final states, as given by

$$E_\mathrm{b} = E_\mathrm{f}(\mathrm{n} - 1) - E_\mathrm{i}(\mathrm{n}), \tag{18}$$

where $E_\mathrm{f}(\mathrm{n} - 1)$ is the final state energy and $E_\mathrm{i}(\mathrm{n})$ is the initial state energy.

The final state energy contains a term related to relaxation, which refers to rearrangement of electrons. There are two types of relaxation: intra-atomic relaxation, which consists of relaxation of electrons within a single atom, and extra-atomic relaxation, in which the surrounding electron density adjusts itself closer to the core hole. The former type of relaxation is mostly due to rearrangement of outer shell electrons that have smaller E_b than the emitted photoelectron. Extra-atomic relaxation, on the other hand, is dependent on the type of material studied. For electrically conducting materials the valence electrons can move between neighbouring atoms to screen the created core hole. For ionically bonded solids, such as calcite and dolomite, the electrons cannot move between atoms, but they can be polarised by the presence of the core hole (Ratner & Castner, 2009). Polarisation does not reduce the binding energy as much as transfer of electrons to screen the core hole. Intra and extra atomic relaxations are two examples of so called final state effects. There are also initial state effects that originate from the ground state of an atom before photoemission process. If the atom has formed chemical bonds with the neighbouring atoms (i.e. the atom is in a different chemical environment), then the binding energy of the original atom will change due to change in oxidation state or, to be more precise, due to change in the electric charge of the atom (Ratner & Castner, 2009). The change in E_b is called a core level chemical shift. It is sometimes described by the equation of the charge potential model (Siegbahn et al., 1967; Ratner & Castner, 2009)

$$\Delta E_\mathrm{b} = \mathrm{k}\Delta q_i + \Delta V_i \ , \tag{19}$$

where ΔE_b is the chemical shift between two states, k is a constant, Δq_i is the change in the charge q on atom i and ΔV_i is the change in the potential of the surrounding atoms, even though the ab initio calculations are more common nowadays. One type of chemical shift is the surface core level shift (SCLS, Citrin et al., 1978), which represents the binding energy difference between core level electrons in the bulk and on the surface. This phenomenon usually originates from the reduced coordination of the surface atoms in comparison to the bulk atoms, which leads to changes in both the charges (charge densities) on the surface atoms and their surrounding potentials. According to the Mönch's model (Mönch, 1986), the charge transfer between cations and anions is the same in the bulk and at the surface. As a consequence, the equation for SCLS becomes

$$\mathrm{SCLS} = E_c^b - E_c^s = \frac{\Delta q \mathrm{e}_0^2}{4\pi\varepsilon_0}\frac{\alpha_\mathrm{b} - \alpha_\mathrm{s}}{d_\mathrm{s}}\ , \tag{20}$$

where E_c^b and E_c^s are the binding energies of bulk and surface atoms, respectively, Δq is the charge transfer between anion and cation, e_0 is the electron charge, ε_0 is the vacuum permittivity, d_s is the anion-cation distance, and α_b and α_s are the bulk and surface Madelung constants, respectively.

Binding energies are characteristic for all elements and electronic orbitals, which allows chemical identification of the sample atoms and their bonding environments. Examples are given in section 5.3. Also, the areas of the peaks can be used to determine atomic concentrations, even though one should bear in mind that the peak intensities have been reported to oscillate at a region extending from the photoionization threshold to several hundred eV higher binding energies (Söderström et al., 2012). If the analysed sample volume is homogeneous, the area of peak *j* from element *i* (I_{ij}) is given by (Ratner & Castner, 2009)

$$I_{ij} = \mathrm{K}T(KE)L_{ij}(\gamma)\sigma_{ij}n_i\lambda(KE)\cos(\theta), \tag{21}$$

where K is an instrumental constant, $T(KE)$ is the transmission function of the analyser, KE is kinetic energy of photoelectrons, $L_{ij}(\gamma)$ is the angular asymmetry factor for orbital *j* of element *i*, σ_{ij} is the photionisation cross-section of peak *j* from element *i* (probability that the incident photon will create a photoelectron from the *j*th orbital of element *i*), n_i is the concentration of element *i* within the sampling depth ($= 3 \cdot \lambda(KE)$), $\lambda(KE)$ is the inelastic mean free path length (the average distance that an electron with a given energy travels between successive inelastic collisions) and θ is (in the case of powder crystalline material with random orientation of the crystallites) the take-off angle of the photoelectrons measured with respect to the surface normal. The concentration of element *i* can be solved from the equation because all other terms can be either measured or calculated. Therefore, atomic concentrations can be determined. In practise, sensitivity factors *S*, that include all terms dependent on sample matrix and instrumentation, simplify the previous equation into (Moulder et al., 1992)

$$C_\mathrm{x} = \frac{n_\mathrm{x}}{\sum n_i} = \frac{I_x / S_x}{\sum I_i / S_i}\ , \tag{22}$$

where C_x is the atomic concentration of element x in the sample, n_x is the number of atoms of the element x per sampling depth, I_x is the number of photoelectrons per second in a specific spectral peak of element x and the summation is over all the elements within the sampling depth.

4.3.1.1 Neutralisation of surface charging

In photoelectron spectroscopy, irradiation of the surface of a sample with X-rays and the subsequent emission of photoelectrons leaves behind a positive charge, which requires neutralisation if the sample has a wide band gap (i.e. the sample is an insulator) (Chusuei & Goodman, 2004). Not only is this positive charging widening the photoelectron peaks making it more difficult to identify the subtle details in the chemical environment of the sample surface, but it is also causing false shifts in binding energies which hinders the identification of the correct binding energy of a peak in a spectrum. The charging phenomena in XPS experiments are the topic for several studies, for example (Gonska et al., 1977; Oswald & Baunack, 1997; Tielsch & Fulghum, 1996; Mukherjee & Mukherjee, 2007; Cazaux, 2010).

Different calibration methods to handle surface charging of insulators have been developed. They can be divided into two groups: charge control method and charge correction method (Baer, 2005), which refer to measures taken during measurements and corrections to the data after acquisition, respectively. During the 1970s it was observed that low energy electrons present in an electron flood gun beam can result in considerable negative charging of the sample (Huchital & McKeon, 1972). Since then, the electron flood gun has been central in charge neutralisation of positive surface charging (Grunthaner & Grunthaner, 1986; Cros, 1992; Baer et al., 2002; Mukherjee & Mukherjee, 2007). The energy of the flood gun electrons has been very low conventionally, because of better neutralization efficiency (Cazaux, 2010). In a method called biased referencing a combination of electron flood gun and a metal dot is used (Edgell et al., 1986). Unfortunately, a flood gun does not always narrow a photoelectron peak (Nesbitt et al., 2004). In the charge correction method, the measured binding energies are corrected with a reference level which is either taken from the literature, or obtained from the surface. In the case of calcite the ways for obtaining a reference value for binding energy correction have included evaporating a small amount of gold on the surface and measuring the 4f line (Stipp & Hochella Jr., 1991; Sommer, 1975), measuring the C 1s line of carbon contamination often referred to as adventitious carbon (Gopinath et al., 2002; Ni & Ratner, 2008) or looking for the binding energy of C 1s in CO_3 carbon from the literature

(Blanchard & Baer, 1992). So far, a reliable reference material has not been found for insulating solids (Sherwood, 2006).

Charging of the surface can also be differential, meaning it is possible for parts of a solid surface to experience a different surface charge as a result of the nature of the sample and the design of the instrument (Sherwood, 2006). It has been reported that neutralization with an electron flood gun is accurate only when the penetration depth of neutralising charges is very close to the distribution in depth of the charges responsible for the charging effects (Cazaux & Lehuede, 1992). With the use of synchrotron radiation, the depth from which the photoelectrons are emitted can be significantly reduced thus making it easier to neutralise vertical differential charging. Neutralisation in general, however, is not easier when synchrotron radiation is used.

In addition to an electron beam/flood, it is possible to use a metal screen positioned 1 to 2 mm above the sample. Using the screen may increase the amount of secondary electrons induced by the photoelectrons (Bryson, 1987). The secondary electrons take part in neutralizing the positive surface potential of an insulator (Cazaux, 2000). According to Cazaux (2000), the ideal solution to smoothen the potential changes would consist of surrounding the specimen with a cloud of electrons that have a kinetic energy as low as possible (with respect to the vacuum level), but the problem is to conceive and build the corresponding attachment.

Recently, it has been shown that the quality of XPS studies of insulators can be at the same level as semi-conductors and metals (Nesbitt et al., 2004), which is promising for the study of non-conducting solids. To the authors' knowledge, no calcite nor dolomite spectrum (with the exception of Doyle et al. (1999), where CaO reacted with CO_2 and produced $CaCO_3$) have been measured previously with synchrotron based XPS. Both dolomite and calcite are insulators, which makes them difficult to study with photoelectron spectroscopic methods. Dolomites indirect electronic band gap has been reported to be ~5.0 eV (Hossain et al., 2011). For calcite, the experimental value of its band gap has been reported to be 6.0 ± 0.35 eV (Baer & Blanchard, 1993).

In this thesis, conventional XPS measurements were carried out at the Laboratory of Materials Science at University of Turku with two different excitation sources: monochromatic Al K_α and non-monochromatic Mg K_α. In the former case, neutralisation of surface charges was implemented through the use of an electron flood gun located at 10 cm from the sample surface. Focusing and deflection enabled more effective neutralisation. The energy of the electrons and sample current were approximately 3 eV and 2 μA, respectively. A current of this magnitude is sufficient for overneutralisation if the current of photoelectrons remains at a few nA. For the latter excitation source, the intensity of the excitation is larger because of the lack of monochromatisation. Therefore, the current from the flood gun is insufficient for neutralisation; electrons emitted from an aluminium window of the x-ray tube are used instead. This results as a more stable situation, even though the sample remains charged.

4.3.1.2 Surface sensitivity

Depending on the definition, a surface could be said to consist of 2 – 10 atomic or molecular layers (Vickerman, 2009). On the metric scale, that may lay between 0.5 and 3 nm. The surface sensitivity of XPS originates from the relatively large probability of inelastic scattering of photoelectrons (Jablonski & Powell, 1999). As shown in Figure 10 (Seah & Dench, 1979), experimental inelastic mean free path of electrons, which stands for the average path length traversed by an electron between two successive inelastic collisions, is a strong function of their kinetic energies. The figure is called universal curve and the version shown is for elements. In addition to inelastic mean free path, $\lambda(KE)$, also mean escape depth (MED) is often used as a measure of surface sensitivity. MED is defined as the average depth normal to the surface from which the specified particles or radiation escape (Jablonski & Powell, 1999).

In XPS spectra, only those photoelectrons that have not lost energy in interactions with other atoms contribute to the photoemission peaks. Those photoelectrons that have experienced inelastic scattering contribute to the background. Unlike in the case of a synchrotron, where the energy of excitation radiation can be tuned (see section 4.3.2), with conventional XPS surface sensitivity can only be enhanced by increasing the angle between detector and surface normal. If the effects of elastic electron scattering are neglected, surface sensitivity can be estimated by equation (Brundle & Roberts, 1973; Bancroft et al., 1979; Jablonski & Powell, 1999; Ratner & Castner, 2009).

$$I = I_0 \left[1 - \mathrm{e}^{-\frac{d}{\lambda(KE)\cos\theta}} \right], \tag{23}$$

where I is intensity (area) of a peak for a surface layer with thickness d, I_0 is intensity (area) of the peak for an infinitely thick sample, $\lambda(KE)$ is the inelastic mean free path of the photoelectrons, which in this equation is that thickness of matter through which 63% of the traversing electrons will lose energy, and θ is the angle between surface normal and take-off angle of photoelectrons.

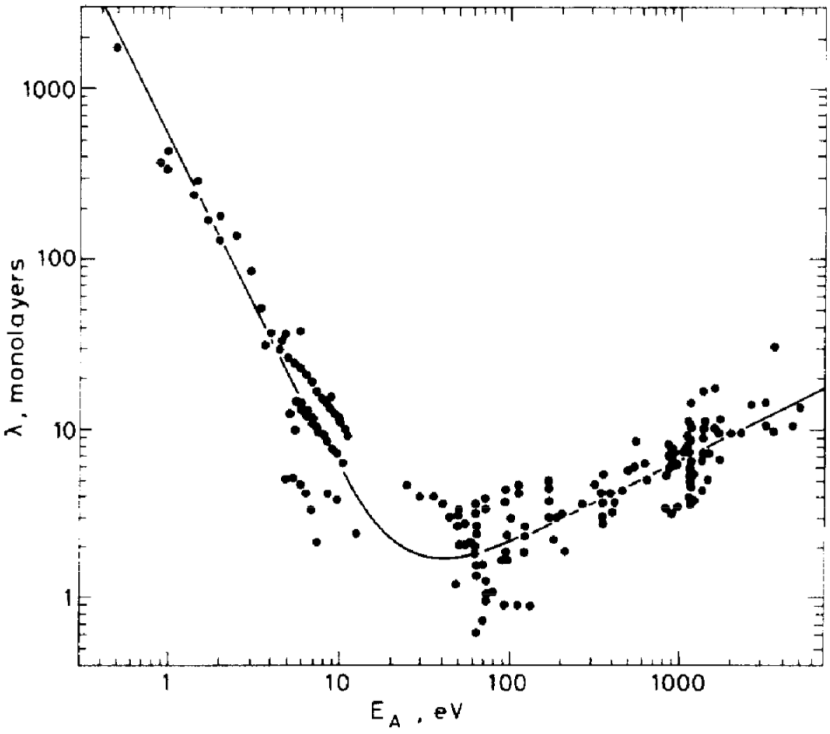

Figure 10. Inelastic mean free path data for elements (Seah & Dench, 1979). The number of atomic layers is plotted as a function of kinetic energy.

4.3.1.3 Fitting of the spectra

In X-ray photoelectron spectroscopy, the acquired spectra are composed of several parameters, such as background formed by inelastically scattered electrons, core photoemission lines, Auger lines, valence lines and satellites. More information on the components is given by for example Moulder et al. (1992) and Ratner & Castner (2009). Fitting of a spectrum aims at dividing it into its components that constitute the spectrum as a whole. For photoelectrons that originate from the s orbital of a given element, a single peak is seen in the spectrum if monochromatic radiation is used. However, chemical shifts caused by different chemical environments or surface core level shifts can produce several peaks with unequal binding energies. In the case of p, d or f orbitals, the spin of an electron can take two values (up or down) that lead to two energetically equivalent final states. A magnetic interaction between the spin of an electron and its orbital angular momentum may lead to a splitting of the energy state, which is seen as two peaks (i. e. a doublet) in the spectrum instead of one (Ratner & Castner, 2009). Such a doublet can be seen, for example, in the Ca 2p spectrum.

The width of a photoemission peak is described by a parameter called full width at half maximum (FWHM). Two major constituents of the shapes of the peaks are the lifetime broadening caused by the lifetime of the core hole left behind by the emitted photoelectron, and the instrumental broadening caused by the spectrometer. The former is defined by the Lorentzian function $L(E)$ given by (Hesse et al., 1999)

$$L(E)=\left\{1+\left[\frac{E-E_0}{\beta}\right]^2\right\}^{-1}, \tag{24}$$

where E is energy, E_0 is the peak position and β stands for ½ of the full width at half maximum. For modelling of the instrumental broadening, a common choice is to use the Gaussian distribution $G(E)$ given by (Hesse et al., 1999)

$$G(E)=\exp\left\{-\ln 2\frac{(E-E_0)^2}{\beta^2}\right\}. \tag{25}$$

The collective influence of Gaussian and Lorentzian distributions is called a Voigt profile. It is defined by convolution of the two according to (Hesse et al., 1999)

$$f(E)=f(L*G)=\int_{-\infty}^{\infty}L(E')G(E-E')dE', \tag{26}$$

where $f(E)$ is the Voigt function and * stands for convolution. In addition, for example the bandwidth of the used radiation (which is never absolutely monochromatic), and energy transfer to the crystal lattice (creation of phonons), can cause further spectral broadening.

In this study, the obtained spectra were analysed with Igor Pro 5.02 software and a special macro package (Kukk, 2000). An integrated Shirley background (Shirley, 1972) or a linear background correction method in combination with a Gaussian-Lorentzian (Voigt) peak shape were used. Often the spectral region was so wide, that the linear background worked better than the integrated one. In the case of calcite, the peak positions were taken from the energies obtained by Blanchard & Baer (1992). For the Ca 2p spectra, the spin-orbit splitting $\Delta_{\text{s-o}}$ = 3.6 eV and the peak intensity ratio of 1:2 were used. For dolomites, Mg $2p_{3/2}$ peak position was set to 50.3 eV (Hu et al., 2006). A spin-orbit splitting of $\Delta_{\text{s-o}}$ = 0.28 eV (Karpus et al., 2006) and an intensity ratio of 1:2 were used.

4.3.2 Synchrotron based XPS (HRXPS)

Instead of an X-ray tube, synchrotron based high resolution XPS (HRXPS) utilises a synchrotron to produce the required excitation radiation. A synchrotron is a particle accelerator where electrons move inside a storage ring with highly relativistic speeds. An injector, which can be, for example, a linear accelerator, is used to feed the storage ring with electrons. Using bending magnets, the electron beam is bended through short arcs that together make up 360 degrees of bending to close the orbit. The pressure inside the storage ring is typically maintained in the range of 10^{-9} to 10^{-10} torr. The storage ring must be made an ultrahigh vacuum (UHV) chamber, since (at MAX II, for example) the electrons travel with almost the speed of light during several hours and their lifetime would be badly influenced by the rest gas. Acceleration of an electron results in emission of photons within a narrow cone in a direction that is perpendicular to the acceleration. When the speed of electrons approaches the speed of light, the cone becomes narrower. A graphical illustration is given by Figure 11. The emitted spectrum of synchrotron radiation extends from the infrared to the hard X-ray parts of the electromagnetic spectrum. The energy lost by the electrons while emitting radiation is replenished by rf cavities, in which electromagnetic fields oscillating at radio frequencies (rf) give longitudinal boosts to the electrons (Winick, 1994). The power of the electromagnetic radiation emitted by the accelerated electrons is proportional to the square of the electron energy and to the square of the magnetic field causing the acceleration (Schlueter, 1994). The desired wavelength (energy) of the excitation radiation can be chosen with a monochromator. In other words, synchrotron radiation is tuneable.

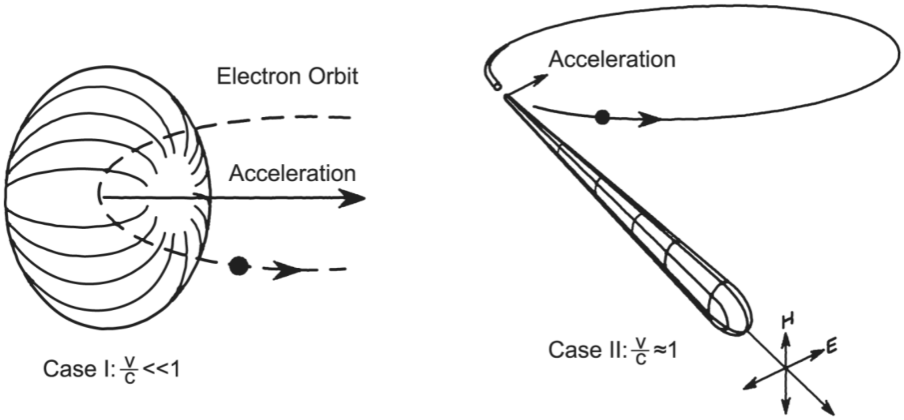

Figure 11. Emission patterns of radiation for electrons in circular (i.e. accelerated) motion for a speed (v) much less than the speed of light (c) (Case I) and for a speed close to the speed of light (Case II). Reproduced from (Winick, 1994) with permission from World Scientific.

4.3.2.1 Beamline I411 at MAX II

The synchrotron based high resolution XPS measurements were carried out at the third generation undulator beamline I411 of MAX II synchrotron laboratory in Lund, Sweden (Bässler et al., 1999; Bässler et al., 2001). After the acceleration inside the storage ring, the electrons reach energy of 1500 MeV. Synchrotron radiation directed to the beamline is created by an undulator, which is a succession of alternating magnetic poles that cause the path of the electrons to alter periodically and therefore emit radiation. The covered photon energy range is from 50 eV to about 1500 eV (Bässler et al., 2001). Spectral brightness for 1-2 GeV undulators is in the order of 10^{16}-10^{18} photons·s^{-1}·mm^{-2}·mr^{-2} (0.1% Bandwidth^{-1})(Winick, 1994). Figure 12 shows the layout of the beamline. Two main components are a modified SX-700 monochromator and a hemispherical Scienta R4000 electron energy analyser, which replaces the SES-200 model. The overall instrumental energy resolutions are 0.1, 0.2 and 0.4 eV for photon energies of 400, 550 and 780 eV, respectively (Tchaplyguine, 2013).

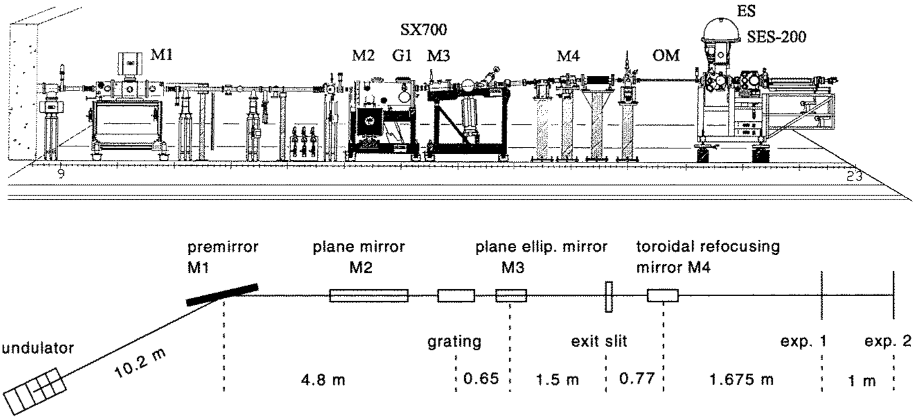

Figure 12. Layout of the beamline I411 at MAX II synchrotron facility. M1 – M4 are focusing mirrors, G1 is a plane grating inside the SX-700 monochromator and OM stands for a free 1 meter section of the beamline (Bässler et al., 1999; 2001). The SES-200 analyser at the end station (ES) has been replaced by a hemispherical Scienta R4000 electron energy analyser.

4.3.2.2 Neutralisation with an electron flood gun

The main difficulty with the flood gun is to adjust it so that the positive charge left behind by the photoelectrons is uniformly and continuously balanced, because otherwise the charging changes (Edgell et al., 1986). More difficulties stem from increase of photon flux, which increases charging effects, although in less proportion (Cazaux, 1999), and the fact that the measured area is larger than what is irradiated by the synchrotron radiation. The optimal parameters for the flood gun were searched by regulating the voltage, the current and the point of electron impact until the minimum core level line width and maximum intensity were reached for either Ca 2p or C 1s, as has been recommended (Bart et al., 1994). Parameters used in HRXPS measurements are shown in Table 3. Both calcite and dolomite samples were mounted into a sample holder with integrated dipole type electron flood gun, and cleaved in UHV. The filament and the extraction aperture were from a PHI 04-085 specimen neutralizer. The flood gun was approximately 10 mm from the sample surface.

Table 3. Measurement parameters for the spectra of calcite (Cc) and dolomite (Dol). V_{fil} and I_{fil} represent the voltage and current over the filament of the electron flood gun, respectively. V_{acc} is the acceleration voltage of the flood gun electrons. Electric current from the flood gun to the sample could not be measured because the sample holder is grounded through the manipulator. E_{pass} is the pass energy of the analyser, *p* is the pressure in the measurement chamber, *step* is the energy step size of the measured spectra and *mask* is a conductive mask described below.

Spectrum	**Cc Ca 2p**	**Dol Mg 2p**
p (mbar)	~ 10^{-8}	~ 10^{-8}
E_{pass} (eV)	100	100, 50, 20
hv (eV)	780, 500	780, 400, 210
mask	gold	no
V_{fil} (V)	1.90	2.20
I_{fil} (A)	2.92	2.98
V_{acc} (V)	3.70	4.20
step (eV)	0.05	0.05

The aim of the neutralisation was to maximise the number of electrons coming from the flood gun to create a so called overneutralisation. If the kinetic energy of the electrons is 3 eV, then the aim is to lower the surface potential to -3 eV, and to keep it there by sending in sufficient amount of electrons to compensate for the photoelectrons. This aims to discrimination of the excess incoming electrons, a constant surface potential and stabilisation of the surface charging.

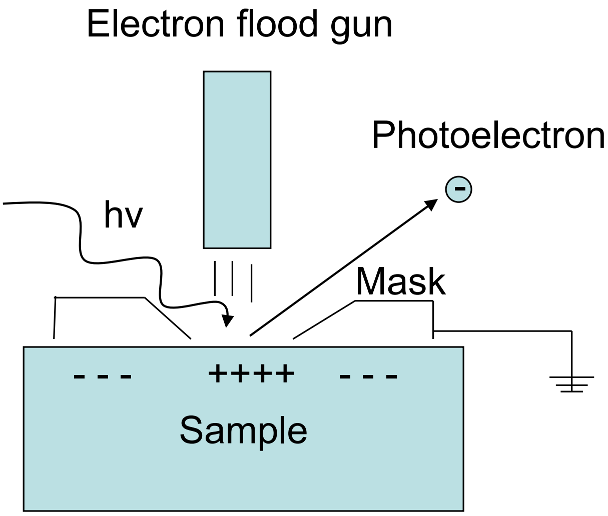

Figure 13. A schematic diagram of the use of both electron flood gun and a conducting mask in neutralisation of surface charging.

For the measurement of Ca 2p spectrum of calcite, a conductive mask (Moulder, 1997) made of gold was situated on top of the sample to improve surface neutralisation, as shown in Figure 13. The mask was grounded and it had a 2 mm hole to limit the measurement area thus making it easier to control the experiment. The conductive copper substrate was also grounded for all experiments. The main idea behind the mask is to prevent flood gun electrons from being repelled by negatively charged areas on the surface and thus achieve a more intensive flow of electrons to the area under analysis.

4.3.3 Scanning Electron Microscopy (SEM)

In Scanning Electron Microscopy (SEM), primary electrons are produced by heating a filament normally composed of W or LaB_6. The beam of electrons is accelerated using a high voltage and focused by a system of electron optics. Collisions between electrons and air molecules would deviate the beam, which is countered by pumping a vacuum inside the SEM chamber.

When primary (incident) electron beam strikes the surface of a sample, three types of electrons emerge: backscattered primary electrons, secondary electrons emitted from the sample atoms, and Auger electrons that originate from the surface. A schematic illustration of the process is depicted in Figure

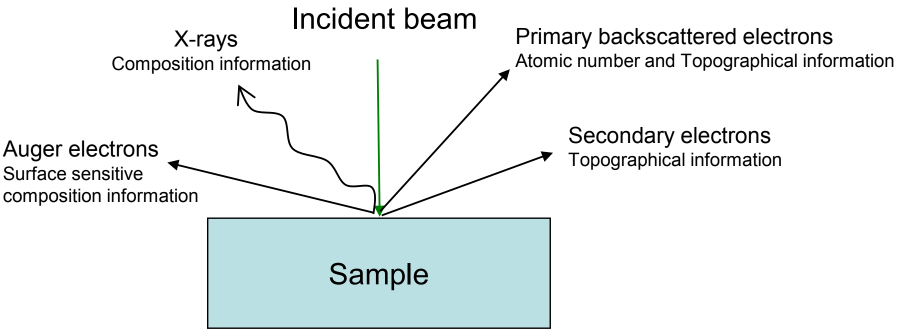

Figure 14. Types or particles emitted or backscattered when incident beam of primary electrons strikes a sample surface in a SEM.

14. The first two types of electrons are used to create images by scanning the primary electron beam over the sample surface and detecting the outgoing electrons. If the backscattering detector is used, brightness in the acquired image varies so that brighter areas represent larger (heavier) atoms, from which the incoming electrons are backscattered more efficiently.

Emitted X-rays constitute a spectrum that can be recorded with an Energy Dispersive X-ray spectrometer (EDX) that is often integrated to the SEM apparatus. From the energies and intensities of the spectral lines one can gain information on the chemical composition of the sample.

4.3.4 X-Ray Diffraction (XRD)

In X-Ray Diffraction, a source of X-rays such as an X-ray tube or a synchrotron, is used to irradiate a sample. X-rays that scatter elastically from atoms of a periodic lattice, can form peaks in a diffractogram if they are in phase. Conditions for this constructive interference are shown in Figure 15. Diffracting atomic planes are separated by a distance d from each other and θ is the angle between X-rays and the atomic planes. Mathematical condition is given by Bragg's law

$$2d\sin\theta = \mathrm{n}\lambda\,, \tag{27}$$

where λ is the wavelength of the X-rays and n is an integer. Angle θ is called the Bragg angle. Equation (27) tells that when the difference in path length of two diffracted waves is equal to an integer multiple of whole wavelengths, constructive interference occurs. If Bragg's law is fulfilled for several Bragg angles, which corresponds to the case of several d-values due to different planes and/or mineral phases, the resulting diffractogram consists of several

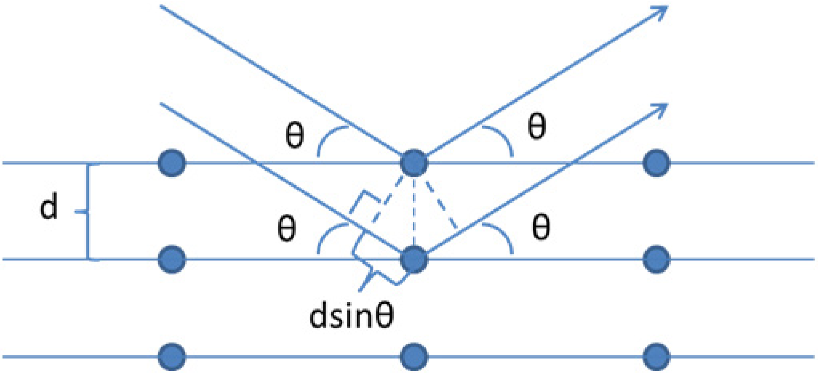

Figure 15. Two originally coherent waves interfere constructively if the difference between their travelled distances equals an integer multiple of wavelengths.

peaks. For all other cases, diffracted waves cancel each other out through destructive interference.

Each mineral has its own characteristic X-ray diffractogram. By comparing the acquired diffractograms to the diffractograms found from databases, one can identify the minerals which represent the (modal) composition of the sample. Rietveld refinement is a technique used to calculate a theoretical diffractogram and to compare it to the measured diffractogram using least squares approach until an optimal fit is achieved (Rietveld, 1969).

4.3.5 X-Ray Fluorescence (XRF)

In XRF, a sample is irradiated with X-rays that have sufficient energy to expel electrons from the atoms. As a result, electrons from higher energy levels are transferred to fill the holes on the lower energy levels. The surplus energy of this transfer is used to emit characteristic fluorescence radiation, where the energy of a photon is equal to the difference of energies between the two involved energy levels. An alternative way to return from the excited state to the ground state is via emission of Auger electrons. The spectrum composed of the emitted characteristic radiation is usually detected by solid-state detectors or gas-filled detectors. The former type is commonly used in energy dispersive XRF (EDXRF), where the radiation emitted by the sample is directly recorded by the detector, while the latter type is mainly used by wavelength dispersive XRF (WDXRF), where the photons emitted from the sample fall on a crystal, which reflects the photons with different wavelengths in different directions. WDXRF has a lower detection limit and a better resolution than EDXRF (Williams, 1987). By measuring the energies of the characteristic photons, it is possible to identify the elements in the sample. By measuring the intensities of the emitted energies, the elemental proportions can be determined. The XRF data shown in this thesis was collected with a WDXRF.

4.3.6 Inductively Coupled Plasma-Mass Spectrometry (ICP-MS) and Inductively Coupled Plasma-Optical Emission Spectrometry (ICP-OES)

Both Inductively Coupled Plasma-Optical Emission Spectrometry (ICP-OES), which is also known as Inductively Coupled Plasma-Atomic Emission Spectrometry (ICP-AES), and Inductively Coupled Plasma-Mass Spectrometry (ICP-MS) take advantage of a quartz glass torch, which by heating creates gas that has some of its atoms or molecules ionised. The samples are originally in liquid forms, but they are injected into the torch by pumping through a capillary tube and converted to an aerosol by a flow of argon gas through a nebuliser in a spray chamber (Walsh, 1997).

For ICP-OES, the ICP torch excites atoms that emit characteristic radiation when the electrons fall back to the lower energy levels. A wide range of spectral emission lines for most elements is produced. The operation temperature is high enough to eliminate most chemical interferences. The emitted photons are directed to the diffraction grating that disperses the incoming beam into separate wavelengths. The intensities of signals of different wavelengths, that are measured simultaneously or sequentially, can be used as a measure of the concentration of the elements (Walsh, 1997).

In ICP-MS, the ICP torch is used as an ion source for a mass spectrometer. From the atmospheric pressure plasma produced by the torch, ions are extracted to the ultra high vacuum mass spectrometer due to a decrease in pressure. The most often used mass analyser in ICP-MS is a quadrupole mass filter that allows only ions with one specific mass to charge ratio to pass to the detector at the time. The detection limit for most elements is typically $<0.01\ \mathrm{ng{\cdot}ml^{-1}}$ (Jarvis, 1997).

4.3.7 Nitrogen physisorption

Nitrogen physisorption is a method that can be used to obtain the surface area of a sample. Before the actual adsorption process takes place, the sample is degassed at an elevated temperature for removal of physisorbed water. The actual physisorption measurement is carried out at 77 K by incrementally increasing the pressure of N_2. As the pressure increases, so does the number of gas molecules adsorbed on the sample surface. Volume of the adsorbed gas is plotted as a function of P/P_0, where P is the equilibrium pressure and P_0 is the saturation pressure. At the first part of this so called isotherm (by the inflection point), a monolayer of adsorbates has covered the surface. This part of the data can be used to calculate the surface area with the help of the BET equation (Brunauer et al., 1938; Lowell et al., 2004)

$$\frac{1}{W\left[\frac{P}{P_0}-1\right]}=\frac{1}{W_mC}+\frac{C-1}{W_mC}\left(\frac{P}{P_0}\right), \tag{28}$$

where W and W_m are the adsorbed weight and monolayer weights, respectively, and C is the BET constant. A plot of $1/W[(P_0/P)-1]$ versus P/P_0 will usually produce a straight line within the range $0.05 \le P/P_0 \le 0.35$. Solving W_m from the equation of the line allows determination of the total surface area, S_i, from the equation

$$S_i=\frac{W_m\overline{\mathrm{N}}A_x}{\overline{M}}, \tag{29}$$

where $\overline{\mathrm{N}}$ is Avogadro's number, A_x is the cross-sectional adsorbate area and $\overline{M}$ is the adsorbate molecular weight (Lowell et al., 2004).

5 Results and discussion

In the following three sections (5.1 – 5.3), a summary of the results of the papers is provided. Instead of presenting the papers one at a time, section 5.1 covers the initial reactivities and the integrated mean specific chemical reaction constants from papers **I**, **II** and **IV**, whereas section 5.2 proceeds with characterisation and the influence of the samples' properties on their initial reactivities (**I**, **II**, **IV**). Photoelectron spectroscopy studies of chemical bonding environments published in paper **III** are summarised in section 5.3.

5.1 Reactivity coefficients and dissolution rates (I, II, IV)

Initial reactivities ($k_{R,0}$) and integrated mean specific chemical reaction constants ($\overline{k_c}$) for the samples are shown in Table 4 for the size fraction 106 – 150 µm. It is emphasised that even though the apparatus used for the dissolution experiments and data collection was the same, the two coefficients $k_{R,0}$ and $\overline{k_c}$ or the two dissolution rates $R_{0,\,1\mathrm{st}}$ and $R_{2\mathrm{nd}}$ cannot be compared with each other because of the different *pH* regions (3.5 – 4 and 4 – 5, respectively) and different mathematical models used to calculate them. In addition, the former coefficient is an initial estimation while the latter gives an integrated mean.

For easier comparison with literature values, Table 4 also shows dissolution rates that are calculated using the two models described in section 4.2. Dissolution rates of the samples in the case of the first order model (that was used to obtain the extrapolated value of $k_{R,0}$ at *pH* 4) were calculated according to

$$R_{0,\,1\mathrm{st}} = \frac{K_0\left[\mathrm{H}^+\right]V_0}{SSA_0 M_0}, \tag{30}$$

where *R* is dissolution rate in mol·cm^{-2}·s^{-1}, *K* is the overall rate coefficient in s^{-1}, [H$^+$] is the bulk concentration of hydrogen ions in mol·l^{-1}, *V* is the liquid volume in l, *SSA* is the specific surface area in cm^2·g^{-1}, *M* is the total mass of the particles in g, and the subscript 0 refers to the extrapolated initial value at *pH* 4.

Dissolution rates of the samples at *pH* 5 in the case of the second order model (that was used to obtain ($\overline{k_c}$) at *pH* 5) were calculated according to (**II**)

$$R = \frac{r_{\mathrm{CaCO}_{3,j}} \cdot v_j}{S_j}, \tag{31}$$

where R is rate of dissolution (mol·cm^{-2}·s^{-1}), $r_{\mathrm{CaCO_3}}$ is the sample consumption rate (mol·cm^{-3}·s^{-1}), v is the volume of the liquid (cm^3), S is the surface area of the reacting particles (cm^2) and j refers to the jth acid addition step. One should note that the model assumes that only $\mathrm{CaCO_3}$ is reacting. The rate calculated using equation (31) has not been extrapolated to the beginning of the experiment. Instead, data from the first acid addition step was used. The sample consumption rate was estimated to be equal to half the hydrogen ion consumption rate $-r_{\mathrm{B}}$ (kmol·m^{-3}·s^{-1}), which was calculated using the equation (**II**)

$$-r_{\mathrm{B}} = -\left[\frac{\mathrm{d}C_{\mathrm{B}}}{\mathrm{d}t}\right] = K_j \cdot C_{\mathrm{B}}^2 , \qquad (32)$$

where C_{B} is the concentration of H$^+$ (kmol·m^{-3}) obtained from rate of change of pH, t is time (s), K is the overall chemical reaction constant (m^3·kmol^{-1}·s^{-1}) and j refers to the jth acid addition step.

As shown by Table 4, dissolution rates and reactivities are generally higher for limestones than dolostones and calcareous rocks, which is in agreement with previous data (Lerman, 1990). The initial reactivities and initial dissolution rates of the calcareous rocks are notably high, which might be due to the flaws of the used model discussed below. It can also be seen that for dolostones, reactivities and dissolution rates varied substantially, whereas for limestones and calcareous rocks, the variation can be primarily explained by relatively large sample standard deviations. Some of the variations in rates and reactivities (and therefore also in sample standard deviations) may be due to the simplicity of the used models. The difficulty with limestones is that their fast dissolution makes it hard to overcome the mass transfer limitations through the diffusion boundary layer, which may have influenced the results. For the limestones and the carbonatite, it is known that dissolution rates were mass transfer controlled, which is why $k_{R,\,0}$ couldn't be obtained (**I**). The initial dissolution rate $R_{0,\,\mathrm{1st}}$ may be too high, because the extrapolation to the initial value was done by fitting an exponential curve to the data points. The shape of the fitted curve is strongly dependent on the first data point whose high value can easily increase the value of the $k_{R,0}$. Use of baffles and other improvements to the experimental method and mathematical models are currently being tested at the Laboratory of Process Design and Systems Engineering at Åbo Akademi University.

Previous studies have also shown that there is variation among dissolution rates. For example, Iceland spar has been shown to have a surface reaction rate only one third of that of the Carrara marble (Rickard & Sjöberg, 1983). Calcite dissolution rates shown by Figure 2 are around 10^{-9} and $5{\cdot}10^{-10}$ mol·cm^{-2}·s^{-1} at pH 4 and 5, respectively. For dolomites, it was pointed out by Anderson (1991), that the surface kinetics may vary between different dolomite samples.

Table 4. Chemical reactivities and dissolution rates of the samples for the size fraction 106 – 150 µm. The numbers are given as arithmetic means of three separate runs including the sample standard deviation. Graphical representations of the numbers are shown as bars underneath them. The initial reactivities ($k_{R,0}$) and the initial dissolution rates ($R_{0,\,1st}$) were calculated using the first order model and extrapolating to zero conversion at *pH* 4. The integrated mean specific chemical reaction constant ($\overline{k_c}$) and the dissolution rate (R_{2nd}) at *pH* 5 were calculated using the second order model. R_{2nd} represents the rate during the first acid addition step, not an extrapolated initial value. (**I, II, IV**, unpublished data).

	Limestones								Carbonatites
	Sedimentary						Metamorphic		Magmatic
	LJJ-04L	LJJ-05L	LJJ-15C	LJJ-21C	LJJ-27C	LJJ-30C	LJJ-09L	LJJ-26C	LJJ-01L
$k_{R,\,0}$ (10^{-1} m·s^{-1})									
$R_{0,\,1st}$ (10^{-8} mol·cm^{-2}·s^{-1})	1.72 ± 0.3	1.83 ± 0.3	1.49 ± 2	1.81 ± 0.2	2.65 ± 2	1.47 ± 0.2	1.37 ± 0.2	1.63 ± 0.3	1.60 ± 0.2
$\overline{k_c}$ (10^{-2} m·s^{-1})	0.29 ± 0.2	0.82 ± 0.9	0.43 ± 0.1	0.89 ± 0.2	0.64 ± 0.2	0.87 ± 0.4	0.37 ± 0.2	0.72 ± 0.04	0.21 ± 0.04
R_{2nd} (10^{-10} mol·cm^{-2}·s^{-1})	0.95 ± 0.7	1.96 ± 3	0.59 ± 0.3	2.29 ± 0.5	2.57 ± 0.5	1.59 ± 0.2	0.49 ± 0.2	1.89 ± 0.2	0.36 ± 0.06

	Dolostones								Calcareous rocks		
	Sedimentary		Metamorphic						Sedimentary		
	LJJ-28C	LJJ-29C	JJ-01C	JJ-02C	JJ-03C	JK-01C	JK-02C	JK-03C	LJJ-06C	LJJ-07C	LJJ-08C
$k_{R,\,0}$ (10^{-3} m·s^{-1})	0.48 ± 0.09	0.35 ± 0.04	1.37 ± 0.33	0.72 ± 0.06	0.21 ± 0.03	0.22 ± 0.05	0.27 ± 0.03	0.85 ± 0.08	1.87 ± 0.3	2.95 ± 0.5	3.98 ± 3
$R_{0,\,1st}$ (10^{-8} mol·cm^{-2}·s^{-1})	0.29 ± 0.05	0.23 ± 0.02	0.60 ± 0.09	0.39 ± 0.04	0.12 ± 0.03	0.15 ± 0.02	0.19 ± 0.02	0.45 ± 0.05	3.51 ± 2	2.58 ± 2	2.33 ± 0.5
$\overline{k_c}$ (10^{-2} m·s^{-1})	0.40 ± 0.1	0.25 ± 0.09	0.27 ± 0.02	0.27 ± 0.02	0.14 ± 0.01	0.08 ± 0.02	0.18 ± 0.04	0.19 ± 0.02	0.12 ± 0.2	0.11 ± 0.09	0.18 ± 0.04
R_{2nd} (10^{-10} mol·cm^{-2}·s^{-1})	0.79 ± 0.09	0.58 ± 0.07	0.80 ± 0.2	0.66 ± 0.04	0.33 ± 0.01	0.25 ± 0.2	0.45 ± 0.08	0.62 ± 0.08	0.73 ± 0.8	0.28 ± 0.03	0.90 ± 1

Similar results were observed by Busenberg & Plummer (1982), who reported that sedimentary dolomites have a faster dissolution rate than those of hydrothermal origin. Figure 3 shows previously obtained dissolution rates for dolomites. At *pH* 4, most of the rates seem to be between 10^{-10} and 10^{-9} ($mol \cdot cm^{-2} \cdot s^{-1}$).

The initial dissolution rates presented in Table 4 are higher than the previously published rates shown in Figures 2 and 3. In the case of calcite-poor metamorphic dolostones (JJ-03C, JK-01C, JK-02C) the differences in dissolution rates compared to the previous results do not seem to be significant, but the dissolution rates of calcareous rocks and limestones are at least one order of magnitude higher than the dissolution rates of pure calcites shown in Figure 2. In addition to the possible error sources originating from extrapolation that were presented above, initial values obtained from powder experiments (like in this thesis) may be faster than rates obtained from cleavage surfaces because grain boundaries having high step and kink density may enhance dissolution (Arvidson et al., 2003). Also, steady state rates would have been slower than the initial rates since the decrease of rates in the beginning of the experiments was exponential. In the case of the second order model, dissolution rates at *pH* 5 are consistent with literature values.

5.2 Characterisation and influence of the properties of the samples to their initial reactivities (I, II, IV)

Figures 16 and 17 show microscope images of thin sections of dolostones, limestones and calcareous rocks. JJ-01C (a metamorphic dolostone), LJJ-04L (a sedimentary limestone) and LJJ-05L (a sedimentary limestone) all show large calcite crystals, even though the first one is a dolostone. Several impurity minerals were detected from the thin sections using a petrographic microscope and EDX. The fact that LJJ-06C (a calcareous rock) reacts slightly faster than LJJ-07C (a calcareous rock) might be due to coarser grain structure of the latter (**I**). Similar conclusions were drawn by Xiang et al. (2009), who reported that low degree of crystallinity (small crystallites) increases dissolution rate. Smaller crystallites increase the amount of grain boundaries having high step and kink density that may enhance dissolution (Arvidson et al., 2003).

X-ray diffraction was used to verify the mineral (modal) composition observed with a petrographic microscope (**I**, **IV**). A good consistency was found. Unlike with a petrographic microscope, with XRD it is relatively straightforward to differentiate calcite from dolomite. Calcite was in fact found from all dolostone samples except LJJ-28C (sedimentary), LJJ-29C (sedimentary) and JK-01C (metamorphic). At the Laboratory of Physical

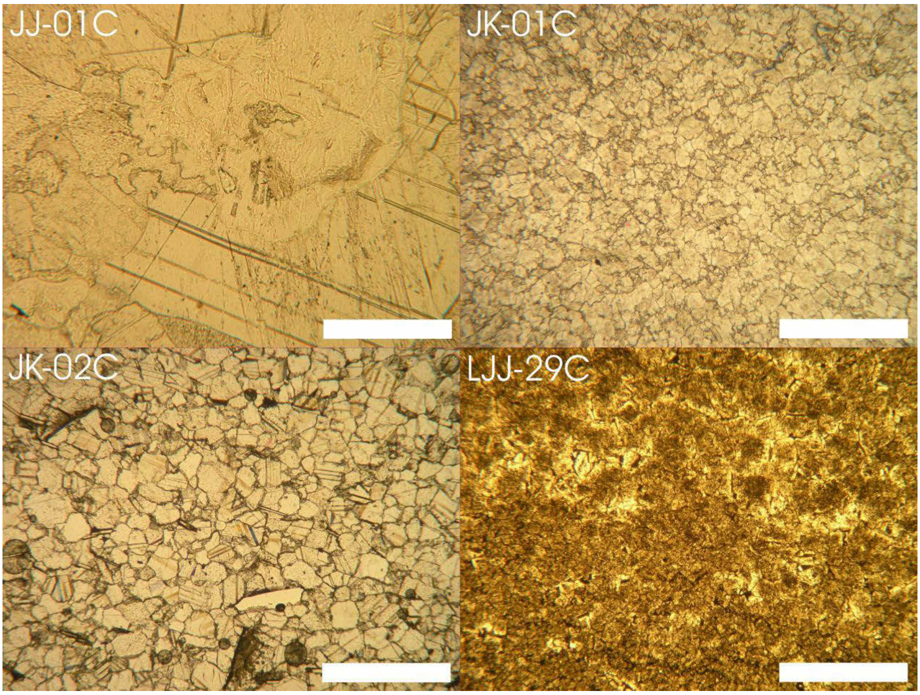

Figure 16. Microscope images of thin sections of the dolostone samples, plane polarised light. Large calcite crystals can be seen in JJ-01C (metamorphic). JK-02C (metamorphic) and JK-01C (metamorphic) consist of smaller calcite and dolomite crystals. Calcite was not detected from the diffractograms of JK-01C and LJJ-29C (sedimentary). Sample LJJ-29 is more fine-grained than the metamorphic ones. The length of the scale bar is 1 mm. (**IV**)

Chemistry at Åbo Akademi University, Rietveld refinement technique was used to estimate proportions of calcite, dolomite and quartz in the dolostone specimens. At the Laboratory of Process Design and Systems Engineering at Åbo Akademi University, a regression model with a significance level of 10% was created for dolostone dissolution. It is given by the equation (**IV**)

$$k_{R,0\ model} = 0.17 + 2.67 \cdot x_{calcite} - 2.46 \cdot x_{quartz} + 0.17 \cdot y_{sediment}, \qquad (33)$$

where $k_{R,0\ model}$ is the modelled initial reactivity, $x_{calcite}$ is the calcite/dolomite ratio in the sample, x_{quartz} is the quartz/dolomite ratio in the sample and $y_{sediment}$ is a binary variable that equals one for sedimentary samples and zero for metamorphic samples.

The modelled initial reactivity $k_{R,0\ model}$ is plotted against the average experimental initial reactivity $k_{R,0\ measured}$ in Figure 18. The straight line is a diagonal, not a fit, which helps the reader to see how consistently the modelled results follow the experimental (measured) ones. The model describes how significant role undolomitised calcite, which dissolves faster than dolomite (Lerman, 1990), has

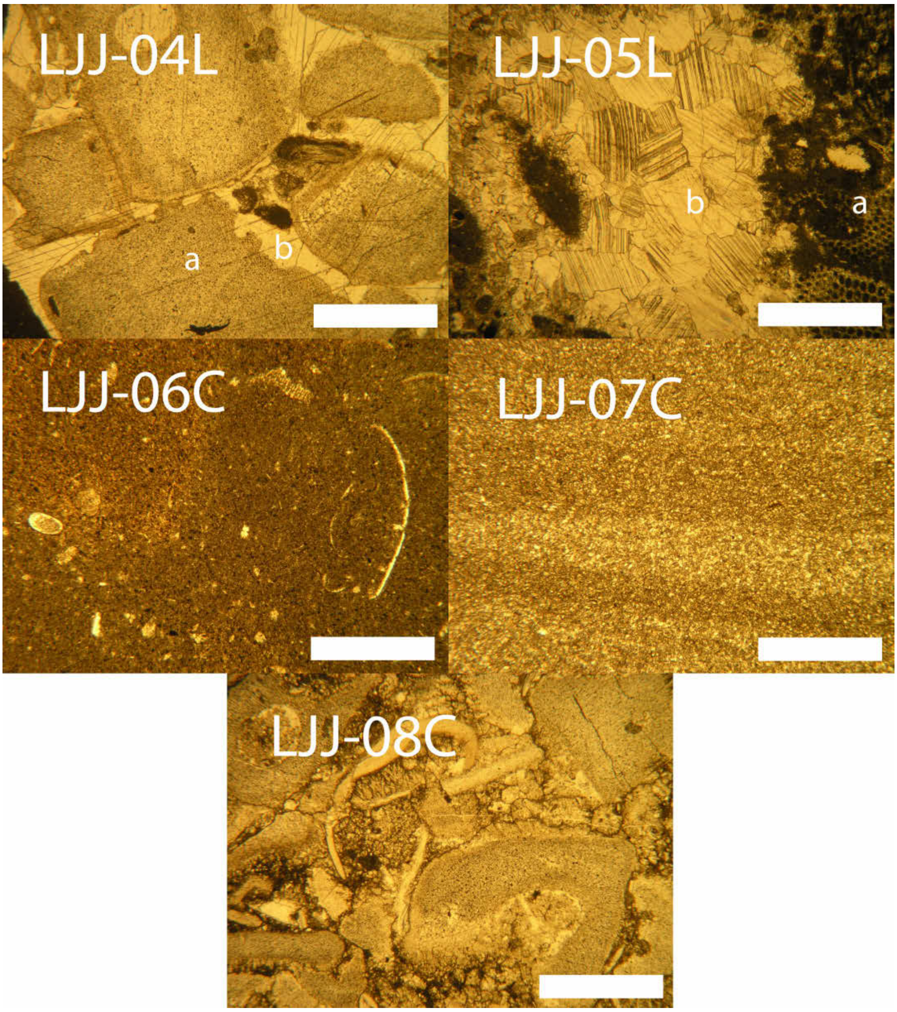

Figure 17. Micrsocope images of thin sections of limestone and calcareous rock samples, plane polarised light. For LJJ-04L (a limestone) and LJJ-05L (a limestone), older fossil-bearing rock (a) and newer re-crystallised calcite (b) can be seen. Also LJJ-06C (a calcareous rock) and LJJ-08C (a calcareous rock) contain fossils. LJJ-07C (a calcareous rock) is laminated and the most fine-grained. The length of the scale bar is 1 mm. (**I**)

in the reactivity experiments of dolostones. If calcite/dolomite ratio is higher than $0.17/2.67 \approx 0.06 = 6\%$, it follows from equation (33) that a metamorphic dolostone is more reactive than a sedimentary dolostone with equal quartz and negligible calcite concentrations. In other words, higher calcite content is suggested to enhance reactivity.

Table 5 shows atomic concentrations (%) of the samples obtained before and after (‘) reactivity experiments using XPS (**I**, **IV** and unpublished data). It seems that chemical (atomic) compositions (unlike mineral (modal) compositions) have a surprisingly small influence on the dissolution rates

- no clear correlation could be observed. Nevertheless, it is suggested that for calcareous rocks, increase in calcium concentration increases reactivity, which is in agreement with previous observations (Siagi & Mbarawa, 2009; Hoşten & Gülsün, 2004). This is likely to be caused by larger amounts of calcite on the surfaces of the dissolving particles. In the case of limestones and dolostones, Ca concentrations did not correlate with the initial reactivities (**IV**) or the integrated mean specific chemical reaction constants (**II**). For dolostones, chemical compositions in general did not seem to have any influence on dissolution. On the other hand, if limestones are compared to dolostones and calcareous rocks, it can be seen that higher Ca concentration results as a faster dissolution rate (see Tables 4 and 5). This is obviously due to higher calcite concentration. For calcareous rocks, calcium concentrations generally decrease relative to impurity concentrations during dissolution, which is attributed to dissolution of calcite. Impurity concentration rises on the surface because calcite dissolves several orders of magnitude faster than silicates (Lerman, 1990).

BET surface areas of the dolostone samples were measured before and after the reactivity experiments. The samples with the largest BET surface areas had also the highest initial reactivities, but the high reactivity was suggested to be in large part due to mineral (modal) composition (high calcite concentration) of those samples. Dissolution rate of calcite has been reported to be faster than that of dolomite (Lerman, 1990). Also, it was observed that BET surface area increases faster than $k_{R,0}$(**IV**).

Euhedral calcite particles are shown in the left panel of Figure 19 (**I**). On the right hand side is an image taken after reactivity experiments, where rounded corners and edges as well as absence of etch pits indicate mass transfer controlled dissolution (Berner, 1978). Figures 20 (**IV**) and 21 (**IV**) show particles of sedimentary and metamorphic dolostones, respectively, both before and after reactivity experiments. Differences of the surfaces between sedimentary and metamorphic samples indicate that there are two different mechanisms for dolostone dissolution. For the sedimentary sample (Figure 20, **IV**), the surface is fully covered with etch pits after dissolution, which not only indicates dissolution at dislocations and grain boundaries, but also suggests that the pits might have an important role in the dissolution process. No chemical differences could be detected with EDX within the areas covered by etch pits, so the formation of etch pits is unlikely caused by chemical or mineralogical impurities. For the metamorphic sample (Figure 21, **IV**), surfaces are smooth and almost free of etch pits although some grooves can be seen. It might be that in this case, dissolution stepwaves (Lasaga & Lüttge, 2001), where the whole surface layer is dissolving, as well as spreading and coalescence of etch pits (Urosevic et al., 2012), might have a central part in the dissolution process.

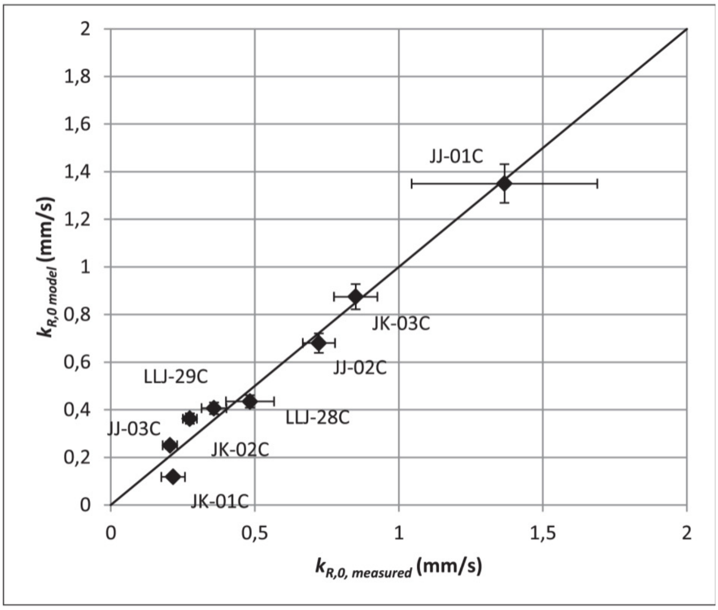

Figure 18. The modelled initial reactivity $k_{R,0\ model}$ versus the average initial reactivity $k_{R,0,measured}$ for dolostone samples. A diagonal (not a fit) is drawn for easier evaluation of the model. (**IV**)

Table 5. The atomic concentration (%) of the studied samples measured before and after reactivity experiments with XPS. The prime symbol (‘), e.g. LJJ-01L’, indicates atomic concentrations measured after reactivity experiments. The percentage for carbon represents only the carbon attributed to CO_3. The column others includes fluorine, chlorine, potassium and cerium. NAN means “not a number” due to division by zero (**I**, **II**, **IV** and unpublished data).

	Rock type	Ca	C	O	Si	Al	K	Fe	Mg	P	Others	Ca/Mg	Fe/Mg
JJ-01C	Dolomite	8.00	10.81	64.35	5.25	3.69	0.00	0.00	7.90	0.00	0.00	1.01	0.00
JJ-01C’		7.44	11.33	62.96	4.12	4.09	0.00	0.00	9.44	0.02	0.59	0.79	0.00
JJ-02C	Dolomite	9.02	13.96	63.57	3.22	3.54	0.00	0.00	6.69	0.00	0.00	1.35	0.00
JJ-02C’		8.64	13.47	63.24	1.83	3.40	0.00	0.00	8.04	0.41	0.96	1.07	0.00
JJ-03C	Dolomite	6.98	10.50	65.47	5.83	4.39	0.00	0.30	6.53	0.00	0.00	1.07	0.05
JJ-03C’		6.41	11.03	63.88	4.43	4.66	0.00	0.83	8.15	3.45	0.49	0.79	0.10
JK-01C	Dolomite	7.96	12.22	65.54	4.34	4.57	0.00	0.51	4.86	0.00	0.00	1.64	0.10
JK-01C’		6.87	9.83	64.72	5.04	4.88	0.00	2.76	5.40	0.25	0.26	1.27	0.51
JK-02C	Dolomite	8.53	13.52	64.46	3.78	3.15	0.00	0.17	6.39	0.00	0.00	1.33	0.03
JK-02C’		7.38	11.03	63.58	4.24	3.62	0.00	1.29	7.52	0.47	0.86	0.98	0.17

	Rock type	**Ca**	**C**	**O**	**Si**	**Al**	**K**	**Fe**	**Mg**	**P**	**Others**	**Ca/Mg**	**Fe/Mg**
JK-03C	Dolomite	8.07	10.26	65.89	5.43	3.42	0.00	0.00	6.94	0.00	0.00	1.16	0.00
JK-03C'		5.65	7.17	64.66	7.99	4.34	0.00	0.48	8.29	0.28	1.16	0.68	0.06
LJJ-01L	Carbonatite	16.55	15.37	60.09	1.79	0.51	0.00	1.20	0.34	3.13	1.02	48.68	3.53
LJJ-01L'		12.11	7.58	66.24	0.77	0.00	0.00	2.66	0.19	7.35	3.10	63.74	14.00
LJJ-04L	Limestone	10.27	10.39	68.54	6.25	3.53	0.00	1.02	0.00	0.00	0.00	NAN	NAN
LJJ-04L'		11.11	9.07	65.96	5.76	3.06	0.00	3.39	0.34	1.03	0.28	32.68	9.97
LJJ-05L	Limestone	15.53	15.18	62.02	4.51	2.45	0.00	0.00	0.30	0.00	0.01	51.77	0.00
LJJ-05L'		11.80	10.67	66.02	5.75	2.18	0.00	2.63	0.20	0.64	0.11	59.00	13.15
LJJ-06C	Calcareous	2.42	1.04	68.70	16.05	9.09	1.43	1.01	0.27	0.00	0.00	8.96	3.74
LJJ-06C'	rock	0.88	0.19	68.10	17.45	9.99	1.45	1.67	0.26	0.00	0.00	3.38	6.42
LJJ-07C	Calcareous	2.92	1.16	71.30	13.66	8.05	0.94	1.49	0.43	0.00	0.02	6.79	3.47
LJJ-07C'	rock	0.92	0.07	68.33	16.45	8.56	0.98	3.65	0.33	0.26	0.46	2.79	11.06
LJJ-08C	Calcareous	7.25	5.03	67.69	11.41	6.99	0.42	0.92	0.29	0.00	0.00	25.00	3.17
LJJ-08C'	rock	5.90	3.69	68.64	9.67	5.66	0.36	3.17	0.00	2.26	0.66	NAN	NAN
LJJ-09L	Limestone	19.64	18.78	59.81	1.17	0.16	0.00	0.00	0.43	0.00	0.01	45.67	0.00
LJJ-09L'		15.25	13.77	65.27	0.84	0.07	0.00	2.40	0.00	2.01	0.39	NAN	NAN
LJJ-15C	Limestone	16.78	16.08	65.36	1.45	0.00	0.00	0.00	0.00	0.00	0.32	NAN	NAN
LJJ-15C'		16.99	15.23	65.34	1.07	0.00	0.00	0.59	0.00	0.16	0.62	NAN	NAN
LJJ-21C	Limestone	13.59	11.82	65.25	6.07	3.28	0.00	0.00	0.00	0.00	0.00	NAN	NAN
LJJ-21C'		14.81	12.37	65.83	2.21	0.90	0.00	2.04	0.00	0.67	1.17	NAN	NAN
LJJ-26C	Limestone	16.94	15.47	65.44	2.15	0.00	0.00	0.00	0.00	0.00	0.00	NAN	NAN
LJJ-26C'		11.92	8.80	66.99	2.84	0.99	0.00	3.66	0.00	3.38	1.41	NAN	NAN
LJJ-27C	Limestone	8.47	6.40	67.64	10.50	4.88	0.82	1.18	0.11	0.00	0.00	79.41	11.09
LJJ-27C'		8.03	5.19	67.54	9.86	3.99	0.53	2.26	0.07	1.31	1.22	109.55	30.77
LJJ-28C	Dolomite	7.73	11.19	64.87	5.62	4.53	0.00	0.55	5.51	0.00	0.00	1.40	0.10
LJJ-28C'		7.73	12.97	63.87	3.13	3.56	0.00	0.73	7.12	0.20	0.69	1.09	0.10
LJJ-29C	Dolomite	7.75	10.99	64.84	5.67	4.31	0.00	0.52	5.92	0.00	0.00	1.31	0.09
LJJ-29C'		8.08	10.65	65.90	3.51	3.55	0.00	0.81	6.19	0.32	0.97	1.31	0.13
LJJ-30C	Limestone	13.09	12.51	65.68	5.91	2.71	0.00	0.00	0.10	0.00	0.00	126.68	0.00
LJJ-30C'		14.36	13.92	66.95	2.38	0.38	0.00	0.90	0.00	0.14	0.98	NAN	NAN

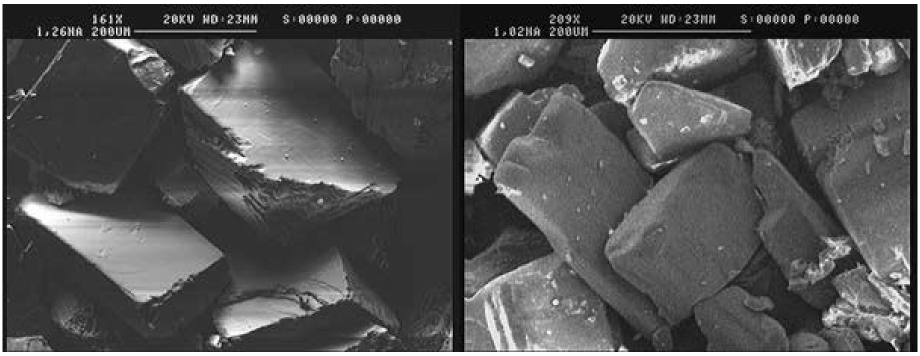

Figure 19. SEM micrographs of euhedral calcite grains from metamorphic limestone LJJ-09L before (left) and after (right) reactivity experiments. The surfaces of the reacted particles (on the right) are characterised by smooth corners and edges, which, along with absence of etch pits, indicates mass transfer controlled dissolution (Berner, 1978). (**I**)

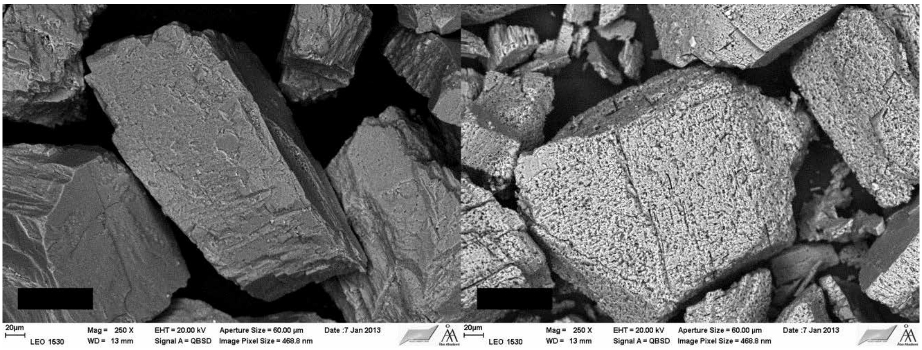

Figure 20. SEM micrographs of sedimentary dolostone LJJ-28C before (left) and after (right) reactivity experiments. The surfaces of the reacted particles (on the right) are characterised by numerous etch pits. The length of the added scale bar is 80 µm. (**IV**)

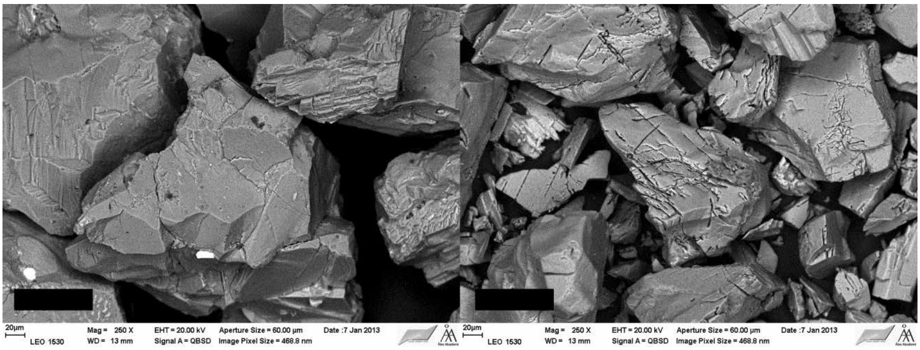

Figure 21. SEM micrographs of metamorphic dolostone JJ-03C before (left) and after (right) reactivity experiments. The surfaces of the reacted particles (on the right) are characterised by smooth planes and grooves. The length of the added scale bar is 80 µm. (**IV**)

5.3 Core-level spectroscopy of calcite and dolomite (III)

Synchrotron based X-ray photoelectron spectroscopy (HRXPS) was used in combination with conventional XPS to gain information on bonding environments of calcite and dolomite. The connection between chemical bonding and dissolution models has been previously demonstrated (Stipp & Hochella, 1991; Van Cappellen et al., 1993). Especially in the synchrotron based experiments, the major obstacle to overcome was the neutralisation of surface charging.

In paper **III**, an Iceland Spar calcite cleaved in UHV was studied with HRXPS and conventional XPS. A cleavage along the $(10\bar{1}4)$ surface was later confirmed with XRD. Figure 22 illustrates two Ca 2p spectra obtained with different excitation energies. A surface component is fitted on the high binding energy side of the main line with a surface core level shift (SCLS) of 0.7 ± 0.1 eV, which is substantially smaller than the previously obtained 1.3 ± 0.2 eV (Stipp & Hochella, 1991). This difference might be due to lower coordination of Ca^{2+} by oxygen, which could be caused by a different amount of steps, edges and kinks on the surface that lead to a different number of Ca-O bonds. Initial and final state effects behind the SCLS are discussed in paper **III** in detail. In the more surface sensitive case shown in the lower panel, the surface component is more pronounced. The full widths at half maximum (FWHM) of the peaks were mostly narrower than in the previous results. The narrow FWHMs and the symmetry of the fitted peaks indicate effective neutralisation of surface charging.

In the Ca 2p spectra acquired with conventional XPS, the SCLS was similar to the HRXPS results. The case with the widest binding energy region is shown in Figure 23. Because of better signal-to-noise ratio than in Figure 22, we were able to study the satellite region in more detail, as can be seen in the enlargement. Two doublets located at about 8.3 and 11.5 eV higher binding energies than the Ca 2p doublet were fitted with a separation of 3.6 eV and an intensity ratio of 2:1, which correspond to the fitting parameters of the Ca 2p doublet. If the given binding energies of the satellites are compared with the dielectric function (ε) of calcite obtained by Medeiros et al. (2007) using density functional theory (DFT) calculations, it can be seen that the conditions of Re $\varepsilon(\omega_p) = 0$ and Im $\varepsilon(\omega)$ having a local minimum, where ω_p is frequency of a bulk plasmon, are met. This interpretation suggests that the satellites occurring at the same binding energies relative to the main peaks are (completely or partly) bulk plasmons also in the C 1s and O 1s spectra of calcite shown in Figures 24 and 25, respectively. In Figure 25, a third satellite is seen. It might be contributed by a second order plasmon, because it is located at approximately twice as far from the CO_3 peak as the first satellite.

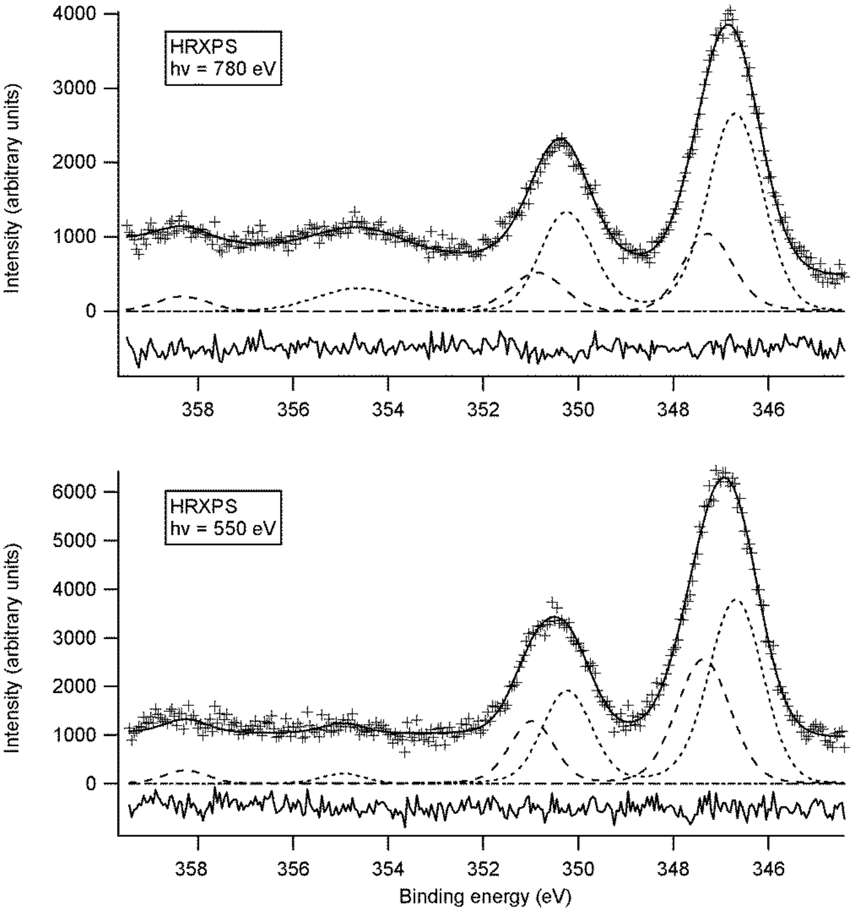

Figure 22. Ca 2p spectra of Iceland spar calcite obtained with HRXPS. The residuals below the peaks show the differences between the raw data and the sum of the fitted components. Markers indicate raw data without background subtraction, dashed lines are the fitted individual components and the thin solid line is the sum of the dashed lines. A linear background correction method was used. (**III**)

In Figure 24, no features can be observed at 6.9 eV lower binding energy from the CO_3 peak, which is the region where carbides (CaC_2) are typically found (Moulder et al., 1992). It turned out that the carbide peaks appear along with the adventitious hydrocarbons, and it was therefore suggested that carbide originates from beam assisted interaction with the hydrocarbons.

A polycrystalline metamorphic dolomite from Reetinniemi, Finland (JJ-02C), was also studied in paper **III**. The sample was cleaved in UHV in order to expose a pristine surface to the experiments. Later, the surface was verified to be dominated by the $(10\bar{1}4)$ plane. Mg 2p and Ca 3s spectra were obtained

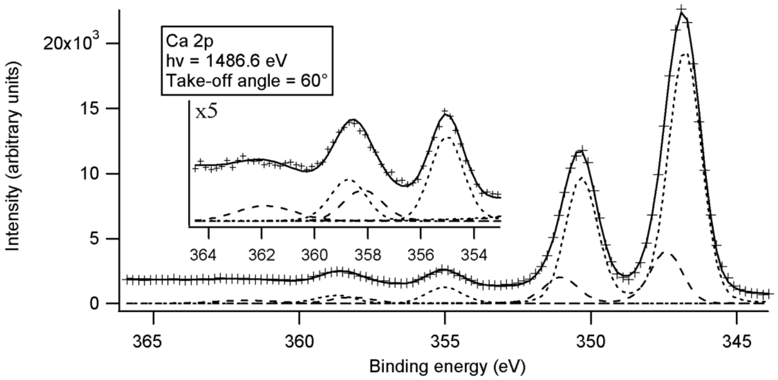

Figure 23. Ca 2p spectra of Iceland spar calcite obtained with conventional XPS. Fivefold enlargement (of the vertical axis) of the satellite region is shown. Markers indicate raw data without background subtraction, dashed lines are the fitted individual components and the thin solid line is the sum of the dashed lines. A linear background correction method was used. (**III**)

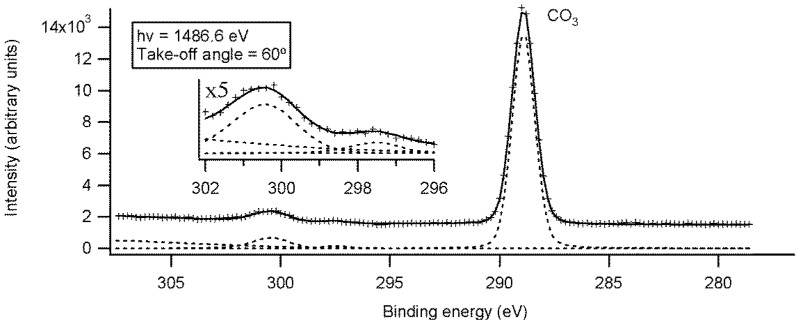

Figure 24. C 1s spectra of Iceland spar calcite obtained with conventional XPS. Fivefold enlargement (of the vertical axis) of the satellite region is shown. Markers indicate raw data without background subtraction, dashed lines are the fitted individual components and the thin solid line is the sum of the dashed lines. The Shirley background correction method was used. (**III**)

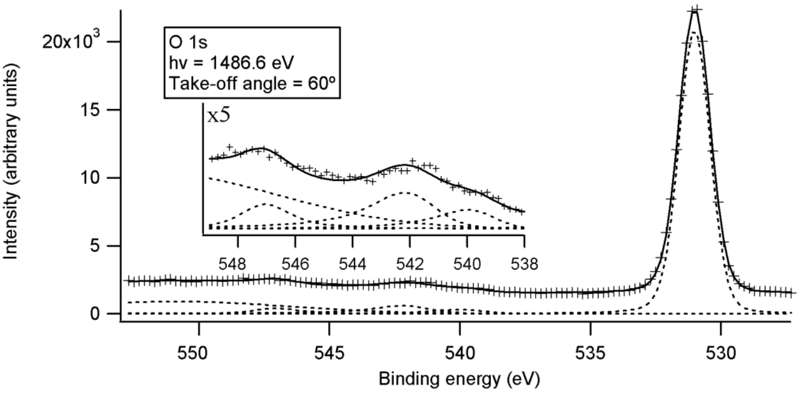

Figure 25. O 1s spectra of Iceland spar calcite obtained with conventional XPS. Fivefold enlargement (of the vertical axis) of the satellite region is shown. Markers indicate raw data without background subtraction, dashed lines are the fitted individual components and the thin solid line is the sum of the dashed lines. The Shirley background correction method was used. (**III**)

with different excitation energies using both HRXPS and conventional XPS, as shown in Figure 26. The components of the Mg 2p doublets have been summed up. In addition to bulk peaks, also surface components were fitted for both Mg 2p and Ca 3s peaks on the high binding energy side of the main line. The SCLS was 0.75 ± 0.05 eV for both cases, which sounds reasonable, because both calcium and magnesium are alkaline earth metals. The similarity with the SCLS in Ca 2p spectrum of calcite is notable. As was calculated in paper **III**, the Mg / Ca atomic ratios did not change as a function of surface sensitivity (excitation energy) for JJ-02C.

Surface core level shifts of 0.7 ± 0.1 eV for Ca 2p spectrum of calcite and 0.75 ± 0.05 eV for Mg 2p and Ca 3s spectra of dolomite were obtained for the $(10\bar{1}4)$ surface. The shift for calcite is 0.6 eV lower than the previously observed value (Stipp & Hochella, 1991). The lower shift might be caused by a smaller number of Ca-O bonds as was discussed in paper **III**. As the outermost atoms and molecules are detached from the calcite $(10\bar{1}4)$ surface during dissolution, the binding energy of the new outermost calcium atoms does not seem to increase as much as has been previously thought. Hopefully, this helps to improve the theoretical models of the calcite and dolomite $(10\bar{1}4)$ surfaces. In the case of the carbide (CaC_2) peak, it was suggested (**III**) that it is a result of beam assisted interaction with adventitious carbon (C-H). Hence, carbide does not seem to be inherently part of the calcite surface.

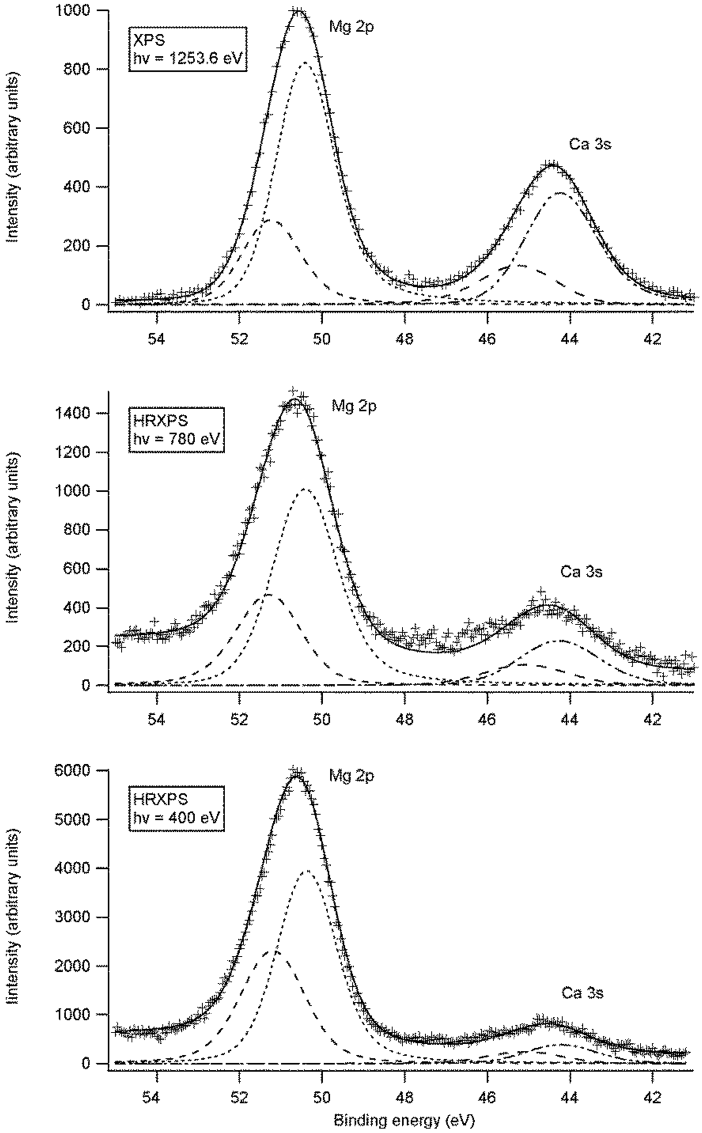

Figure 26. Mg 2p and Ca 3s spectra of JJ-02C obtained with HRXPS. Markers indicate raw data without background subtraction, dashed lines are the fitted individual components and the thin solid line is the sum of the dashed lines. The Shirley background correction method was used. (**III**)

6 Conclusions

Coal-fired power plants continue to be an important source of energy throughout the world even though large scale investments and efforts for adding the share of renewable energy sources are constantly made. A pivotal factor for wet Flue Gas Desulphurisation (FGD) of the emissions is dissolution of limestones used as raw materials. Without FGD, emission of sulphur dioxide leads to reaction with water and oxygen, and production of sulphuric acid (H_2SO_4), which subsequently contributes to the formation of hazardous acid rains. Another important application of knowledge covering dissolution is in construction industry, where preservation of limestones and dolostones used as building stones is an essential issue. In wet FGD, high reactivity (dissolution rate) is a desired property, whereas in construction industry, low reactivity is looked for.

The reactivity experiments done for limestones and dolostones indicate that there is no single dissolution rate or chemical reactivity for these types of samples (**I**, **II**, **IV**, unpublished data). In general, dissolution rates and reactivities are higher for limestones than dolostones and calcareous rocks. Limestones dissolve so fast that it is not easy to overcome the mass transfer limitations through the diffusion boundary layer. This may contribute to the relatively high sample standard deviations of dissolution rates (in Table 4), which are often one or two orders of magnitude higher for limestones and calcareous rocks than for dolostones. When the *pH* region 3.5 – 4 and a first-order rate equation were used, it was observed that limestone dissolution is controlled by mass transfer (**I**). In paper **II**, the *pH* region was raised to 4 – 5, and a first-order rate equation of hydrogen ion consumption was replaced by a second-order equation. This higher *pH* should lead to chemical kinetics controlled dissolution, and a higher-order rate equation should improve the dissolution model. The dissolution rates obtained with this second-order model were more consistent with literature values than the rates obtained with the first-order model at lower *pH*. However, further development of the instrumentation and the model are still needed.

Characterisation of the samples revealed that chemical compositions do not correlate with the reactivities. However, when limestones are compared to calcareous rocks and dolostones, it can be seen that limestones, which obviously have higher calcite concentrations, and therefore also higher Ca concentrations, have higher reactivities and faster dissolution rates.

The acquired sample standard deviations for limestones and calcareous rocks were too high for a meaningful ranking of limestones according to their dissolution rates or integrated mean specific chemical reaction constants (paper **II**, unpublished data), but for dolostones, a ranking based on the initial reactivities (**IV**) and starting from the most reactive (fastest dissolving) sample goes as follows:

1) metamorphic dolostones with calcite/dolomite ratio higher than about 6%
2) sedimentary dolostones without calcite
3) metamorphic dolostones with calcite/dolomite ratio lower than about 6%

In table 4, reactivities and dissolution rates obtained with two different models and *pH* regions were shown. Dissolution rates obtained using the second order model at *pH* 5 were consistent with literature values, whereas the initial rates obtained with the first order model at *pH* 4 were repeatedly higher than the previous rates, which may originate from extrapolation of the reactivity to the initial value or from the simplicity of the first order model.

A regression model taking into account the concentrations of dolomite, calcite and quartz in the sample as well as the type of the sample (sedimentary or metamorphic), has been presented for the initial reactivities of dolostones. Sedimentary dolostones dissolved faster than metamorphic ones, unless the latter had calcite/dolomite ratio higher than about 6% (according to the model) to enhance dissolution (**IV**). In addition, it is assumed that a higher BET surface area and a finer grain structure enhance dissolution rates. However, in this work, no certain correlation was found.

Comparison between the dissolved surfaces of sedimentary and metamorphic dolostones indicates that there are different dissolution mechanisms for the two groups of samples. Plane waves as well as spreading and coalescence of etch pits might have a pronounced (rate controlling) part in the dissolution of metamorphic dolostones, whereas in the case of sedimentary dolostones, growth and coalescence of individual etch pits might control the dissolution. The surfaces of the sedimentary dolostones have become porous during the dissolution experiments (**IV**).

A more profound understanding of dissolution might come through information concerning electronic structure and bonding environments of the materials, which can be acquired using X-ray photoelectron spectroscopy. Unfortunately both calcite and dolomite are insulators, which makes recording of spectra more difficult. As shown in this thesis, a successful neutralisation is nevertheless possible when using synchrotron radiation. The obtained spectra indicate that carbide (CaC_2) is not a fundamental part of a calcite surface, but might instead originate from beam assisted interaction with hydrocarbons. The acquired surface core level shifts in Ca 2p spectra of calcite (0.7 ± 0.1 eV), and Mg 2p and Ca 3s spectra of dolomite (0.75 ± 0.05 eV), may help to create more accurate theoretical models for calcite and dolomite $(10\bar{1}4)$ surfaces. Also, experimental verifications for density functional theory based calculations of the energies of collective excitations of electrons (i.e. bulk plasmons) have been presented for Ca 2p, C 1s and O 1s spectra of calcite (**III**).

Future challenges for the apparatus located at the Laboratory of Process Design and Systems Engineering at Åbo Akademi University include overcoming the mass transfer limitations at lower *pH* (≤ 4) and achieving a better repeatability. Regarding characterisations of limestones and dolostones, analyses of chemical bonds using a Fourier Transform Infrared spectroscopy (FTIR) or in-situ studies of dissolving surfaces with Atomic Force Microscopy (AFM)might lead to a better understanding of what factors influence the varying dissolution rates, and why are the surfaces of sedimentary and metamorphic dolostones so different after dissolution.

Acknowledgements

Because the topic of this thesis is multidisciplinary by nature, I cannot thank a single person for introducing the whole field. However, I can thank i) my supervisor Olav "Joffi" Eklund for letting me in to the world of rocks, his motivating speeches and his fully functioning open door policy; ii) my supervisor Jarkko Leiro for showing me what can be done with photoelectron spectroscopy, his endless patience and scrupulous attention to details; iii) Edwin Kukk for teaching me what a surface is, picking up two absolutely crucial samples for this thesis and his expertise with Igor Pro; iv) Jarl Ahlbeck for explaining what happens to a limestone particle in an acidic solution and the original development of the experimental method for measuring limestone reactivities; and v) Ron Zevenhoven for running the CARETECH group and helping me with occasional scientific problems.

An important part for carrying out the research during the past years has been played by Frej Bjondahl and Claudio Carletti, who have provided me with reactivity data. A tremendous technical and practical assistance has been available through the work of Pia Sonck-Koota, Arto Peltola, Sören Fröjdö, Maxim Tchaplyguine, Kenneth Fjäder, Synnöve Hollsten, Jan-Henrik Smått, Linus Silvander, Paul Ek, Sten Lindholm and especially Markku Heinonen. Sari Granroth, Taina Laiho and Carl Ehlers are thanked for their support and help with scientific problems. For fruitful collaboration I acknowledge Kristian Gunnelius, Tom Lundin, Cataldo De Blasio, Tapio Westerlund, Jani Jäsberg, Jaakko Kara and Ville Viitanen. I've enjoyed working at both Materials Science (University of Turku) and Geologi och Mineralogi (Åbo Akademi University). I want to express my gratitude to my fellow (present and former) PhD students Sonja Sjöblom, Ari Brozinski, Amélie Beucher, Miradije Rama and Miriam Nystrand for providing a great working atmosphere in four languages (sometimes during the same coffee break). Thanks also to Juha Kauhanen for the bar (i.e. the rod) and Erik Sturkell for letting me escape from writing to teaching geophysics.

I am grateful to the two reviewers of this thesis, Alvar Soesoo and Svante Svensson, for their valuable comments that helped to improve this thesis. In addition, several other people within the academia have given me insightful comments and thought-provoking ideas. For these I thank Susan Brantley, Henrik Grenman, Andreas Lüttge, Jonathan Icenhower, Are Korneliussen and Erik Jonsson.

This work would not have been possible without rocks. Therefore I acknowledge Seppo Gehör, Leif Johansson, Sma Minerals corp., North Cape Minerals corp. (Thomas Hellsten), Nordkalk corp. (Kenneth Fjäder, Gerhard

Hakkarainen, Synnöve Hollsten), Technical University of Tallinn (Alvar Soesoo, Olle Hints), Yara corp. (Olli Härmälä) and Finn Nickel corp. (Olli-Pekka Isomäki).

Most of the financial support has been provided by Academy of Finland through its Sustainable Energy program (2008-2011). Additional and much needed scholarships were granted by K.H. Renlund's Foundation, Ella and Georg Ehrnrooths' Foundation, Swedish Cultural Foundation in Finland and Rector of Åbo Akademi University. Thank you.

There is life also outside academia, which is vital for a PhD student's recovery and recharging. I'd like to thank all my friends and relatives for having good times with me, especially penkkaajat, lenkkeilijät and those who play Domppa. My parents Päivi and Risto, and my brother Jukka are acknowledged for their endless support and encouragement. Finally, my deepest thanks go to my beloved wife Helena. Thank you for making my life more interesting.

Turku, December, 2014

Lauri Järvinen

References

B. Adnadjevic, A. Popovic, Fuel Process. Tech. 89 (2008) 773-776.

J. Ahlbeck, T. Engman, S. Fälten, M. Vihma, Chem. Eng. Sci. 48 (1993) 3479-3484.

J. Ahlbeck, T. Engman, S. Fältén, M. Vihma, Chem. Eng. Sci. 50 (1995) 1081-1089.

T. Akiyama, K. Nakamura, T. Ito, Phys. Rev. B 84 (2011) 085428.

M. Alkattan, E.H. Oelkers, J.-L. Dandurand, J. Schott, Chem. Geol. 190 (2002) 291-302.

D.C. Anderson, P. Anderson, A.K. Galwey, Fuel 74 (1995) 1024-1030.

M.S. Anderson, SPE Prod. Eng. 6 (1991) 227-232.

R.S. Arvidson, I.E. Ertan, J.E. Amonette, A. Lüttge, Geochim. Cosmochim. Acta 67 (2003) 1623-1634.

R.S. Arvidson, M. Collier, K.J. Davis, M.D. Vinson, J.E. Amonette, A. Lüttge, Geochim. Cosmochim. Acta 70 (2006) 583-594.

D.R. Baer, D.L. Blanchard Jr., Appl. Surf. Sci. 72 (1993) 295-300.

D.R. Baer, M.H. Engelhard, D.J. Gaspar, A.S. Lea, C.F. Windisch Jr., Surf. Interface Anal. 33 (2002) 781-790.

D.R. Baer, Surf. Interface Anal. 37 (2005) 524-526.

Z. Bakri, A Zaoui, Phys. Status Solidi B 248 (2011) 1894-1900.

G.M. Bancroft, J.R. Brown, W.S. Fyfe, Chem. Geol. 25 (1979) 227-243.

F. Bart, M.J. Guittet, M. Henriot, N. Thromat, M. Gautier, J.P. Duraud, J. Electron Spectrosc. Relat. Phenom. 69 (1994) 245-258.

P. Barton, T. Vatanatham, Environ. Sci. Tech. 10 (1976) 262-266.

A.F.M. Barton, S.R. McConnel, Chem. Australia 46 (1979) 427-433.

R.A. Berner, Am. J. Sci. 278 (1978) 1235-1252.

D.L. Blanchard Jr., D.R. Baer, Surf. Sci. 276 (1992) 27-39.

J. G. Boguski, Ueber die Geschwindigkeit der chemischen Vorgänge, in Berichte der Deutschen Chemischen Gesellschaft zu Berlin (Ed: H. Wichelhaus), Ferd. Dümmlers Verlagsbuchhandlung, Harrwitz und Gossmann, Berlin, 1876, pp. 1646-1652.

D.R. Boomer, C.C. McCune, H.S. Fogler, Rev. Sci. Instrum. 43 (1972) 225-229.

B.P. Boudreau, Geophys. Res. Lett. 40 (2013) 1-5.

S.L. Brantley, Kinetics of Mineral Dissolution, in Kinetics of Water-Rock Interaction (Eds: S.L. Brantley, J.D. Kubicki, A.F. White), Springer, New York, 2008, pp. 151-210.

M.G. Brik, Phys. B 406 (2011) 1004-1012.

S. Brunauer, P. H. Emmett, E. Teller, J. Am. Chem. Soc. 60 (1938) 309-319.

C.R. Brundle, M.W. Roberts, Chem. Phys. Lett. 18 (1973) 380-381.

C.E. Bryson III, Surf. Sci. 189/190 (1987) 50-58.

E. Busenberg, L.N. Plummer, Am. J. Sci. 282 (1982) 45-78.

E. Busenberg, L.N. Plummer, in Studies of Diagenesis (Ed: F.A. Mumpton), U.S. geological Survey Bulletin 1578, 1986, pp. 139-168.

M. Bässler, J.-O. Forsell, O. Björnholm, R. Feifel, M. Jurvansuu, S. Aksela, S. Sundin, S.L. Sorensen, R. Nyholm, A. Ausmees, S. Svensson, J. Electron Spectrosc. Relat.Phenom. 101-103 (1999) 953-957.

M. Bässler, A. Ausmees, M. Jurvansuu, R. Feifel, J.-O. Forsell, P. de Tarso Fonseca, A. Kivimäki, S. Sundin, S.L. Sorensen, R. Nyholm, O. Björnholm, S. Aksela, S. Svensson, Nucl. Instr.And Meth. A 469 (2001) 382-393.

K. Caldeira, M.E. Wickett, Nature 425 (2003) 365.

C. Carletti, F. Bjondahl, C. de Blasio, J. Ahlbeck, L. Järvinen, T. Westerlund, Environ. Prog. Sustain. Energy 32 (2013) 663-672.

J. Cazaux, P. Lehuede, J. Electron Spectrosc. Relat.Phenom. 59 (1992) 49-71.

J. Cazaux, J. Electron Spectrosc. Relat.Phenom. 105 (1999) 155-185.

J. Cazaux, J. Electron Specrosc. Relat.Phenom. 113 (2000) 15-33.

J. Cazaux, J. Electron Spectrosc. Relat.Phenom. 178-179 (2010) 357-372.

P.K. Chan, G.T. Rochelle, in Flue Gas Desulfurization (Ed: M.J. Comstock), ACS Symp. Ser. 188, 1982, pp. 75-97.

J. Chen, H. Yao, L. Zhang, Fuel 102 (2012) 386-395.

J. Cheng, J. Zhou, J. Liu, Z. Zhou, Z. Huang, X. Cao, X. Zhao, K. Cen, Prog. Energy Combust. Sci. 29 (2003) 381-405.

L. Cheng, N.C. Sturchio, J.C. Woicik, K.M. Kemner, P.F. Lyman, M.J. Bedzyk, Surf. Sci. 415 (1998) L976-L982.

L. Chou, R.M. Garrels, R. Wollast, Chem. Geol. 78 (1989) 269-282.

C.C. Chusuei, D.W. Goodman, in Encyclopedia of physical science and technology(Ed: R.A. Meyers), Elsevier B. V., ScienceDirect, 2004, pp. 921-938.

P.H. Citrin, G.K. Wertheim, Y. Baer, Phys. Rev. Lett. 41 (1978) 1425-1428.

A. Cros, J. Electron Spectrosc. Relat. Phenom. 59 (1992) 1-14.

K. Dam-Johansen, K. Østergaard, Chem. Eng. Sci. 46 (1991) 827-837.

P. Davini, Fuel 79 (2000) 1363-1369.

J.A. Davis, D.B. Kent, in Mineral-water interface geochemistry, Reviews in Mineralogy vol 23 (Eds: M.F. Hochella, Jr, A.F. White), Mineralogical Society of America, Washington DC, 1990, pp. 177-260.

C.S. Doyle, T. Kendelewicz, X. Carrier, G.E. Brown, JR., Surf. Rev. Lett. 6 (1999) 1247-1254.

O. W. Duckworth, S. Martin, Am. Mineral. 89 (2004) 554-563.

M.J. Edgell, D.R. Baer, J.E. Castle, Appl. Surf. Sci. 26 (1986) 129-149.

M.G. Evans, M. Polanyi, Trans. Faraday Soc. 31 (1935) 875-894.

H. Eyring, J. Chem. Phys. 3 (1935) 107-115.

P. Fellner, V. Khandl, Chem. Papers 53 (1999) 238-241.

C. Fischer, A. Lüttge, Am. J. Sci. 307 (2007) 955-973.

C. Fischer, R.S. Arvidson, A. Lüttge, Geochim. Cosmochim. Acta 98 (2012) 177-185.

P. Galuszka, The New York Times, 14/11/12, Available at: http://www.thegwpf.org/china-india-building-4-coal-power-plants-week/ (Accessed on 21st May 2014).

M. Gautelier, E.H. Oelkers, J. Schott, Chem. Geol. 157 (1999) 13-26.

M. Gautelier, J. Schott, E.H. Oelkers, Chem. Geol. 242 (2007) 509-517.

J.-M. Gautier, E. H. Oelkers, J. Schott, Geochim. Cosmochim. Acta 65 (2001) 1059-1070.

J. Geyssant, in Calcium Carbonate – From the Cretaceous Period into the 21st Century (Eds: F.W. Tegethoff, J. Rohleder, E. Kroker), Birkhäuser Verlag, Basel, Switzerland, 2001, pp. 1-52.

H. Gonska, H.J. Freund, G. Hohlneicher, J. Electron Spectrosc. Relat.Phenom. 12 (1977) 435-441.

C.S. Gopinath, S.G. Hegde, A.V. Ramaswamy, S. Mahapatra, Mater. Res. Bull. 37 (2002) 1323-1332.

F.J. Grunthaner, P.J. Grunthaner, Mater. Sci. Rep. 1 (1986) 65-160.

B.B. Hansen, S. Kiil, J.E. Johnsson, Fuel 90 (2011) 2965-2973.

R. Hesse, T. Chassé, R. Szargan, Fresenius J. Anal. Chem. 365 (1999) 48-54.

S.R. Higgins, X. Hu, Geochim. Cosmochim. Acta 69 (2005) 2085-2094.

P.E. Hillner, S. Manne, A.J. Gratz, P.K. Hansma, Ultramicrosc. 42-44 (1992) 1387-1393.

F.M. Hossain, B.Z. Dlugogorski, E.M. Kennedy, I.V. Belova, G.E. Murch, Comput. Mater. Sci. 50 (2011) 1037-1042.

Ç. Hoşten, M. Gülsün, Miner. Eng. 17 (2004) 97-99.

G. Hu, K. Dam-Johansen. S. Wedel, AIChE J. 57 (2011) 1607-1616.

X. Hu, P. Joshi, S. M. Mukhopadhyay, S. R. Higgins, Geochim. Cosmochim. Acta 70 (2006) 3342-3350.

M. Hua, B. Wang, L. Chen, Y. Wang, V.M. Quynh, B. He, X. Li, Fuel 89 (2010) 1812-1817.

D.A. Huchital, R.T. McKeon, Appl. Phys. Lett. 20 (1972) 158-159.

A. Jablonski, C.J. Powell, J. Electron Spectrosc. Relat.Phenom. 100 (1999) 137-160.

K.E. Jarvis, in Modern Analytical Geochemistry: An Introduction to Quantitative Chemical Analysis Techniques for Earth, Environmental and Materials Scientists (Ed: R. Gill), Addison Wesley Longman Limited, Singapore, 1997, pp. 171-187.

S.E. Kaczmarek, D.F. Sibley, Sediment. Geol. 240 (2011) 30-40.

J. Kaminski, Appl. Energy 75 (2003) 165-172.

N. Karatepe, Energy Sources 22 (2000) 197-206.

S. Kiil, M.L. Michelsen, K. Dam-Johansen, Ind. Eng. Chem. Res. 37 (1998) 2792-2806.

E. Kukk, Spectral Analysis by Curve Fitting Macro Package /SPANCF/2000, available at: http://www.physics.utu.fi/en/department/materials_research/materials_science/Fitting.html (Accessed on 2nd November 2012).

K.J. Laidler, M.C. King, J. Phys. Chem. 87 (1983) 2657-2664.

A.C. Lasaga, in Kinetics of Geochemical Processes, Reviews in Mineralogy vol. 8 (Eds: A.C. Lasaga, R.J. Kirkpatrik), Mineralogical Society of America, Washington DC, 1981, pp. 135-169.

A.C. Lasaga, A. Lüttge, Sci. 291 (2001) 2400-2404.

A. Lerman, in Aquatic chemical kinetics – Reaction rates of processes in natural waters (Ed: W. Stumm), John Wiley & Sons, Inc., New York, 1990, pp. 505-534.

C.-F. Liu, S.-M.Shih, R.-B. Lin, Chem. Eng. Sci. 57 (2002) 93-104.

Z. Liu, D. Yuan, W. Dreybrodt, Environ. Geol. 49 (2005) 274-279.

E.A. Lowe, L.K. Evans, J. Cleaner Prod. 3 (1995) 47-53.

S. Lowell, J.E. Shields, M.A. Thomas, M. Thommes, Characterization of Porous Solids and Powders: Surface Area, Pore Size and Density, Kluwer Academic Publishers, Dordrecht, The Netherlands, 2004.

H. Lukkarinen, in Description to the Bedrock Map of Central Fennoscandia, (Mid-Norden) (Eds: T. Lundqvist & S. Autio), Geol. Surv. Finland Spec. Pap. 28(2000) 12-25.

K. Lund, H.S. Fogler, C.C. McCune, Chem. Eng. Sci. 28 (1973) 691-700.

A. Lüttge, E. W. Bolton, A. C. Lasaga, Am. J. Sci. 299 (1999) 652-678.

A. Lüttge, U. Winkler, A.C. Lasaga, Geochim. Cosmochim. Acta 67 (2003) 1099-1116.

A. Lüttge, Am. Mineral. 90 (2005) 1776-1783.

A. Lüttge, J. Electron Spectrosc. Relat.Phenom. 150 (2006) 248-259.

A. Lüttge, R. S. Arvidson, C. Fischer, Elem. 9 (2013) 183-188.

H.G. Machel, in Encyclopedia of Geology (Eds: R.C. Selley, L.R.M. Cocks, I.R. Plimer), Elsevier Ltd., 2005, pp. 79-94.

B. Mason, L.G. Berry, Elements of Mineralogy, W. H. Freeman and Company, San Francisco, 1968.

S.K. Medeiros, E.L. Albuquerque, F.F. Maia Jr., E.W.S. Caetano, V.N. Freire, J. Phys. D: Appl. Phys. 40 (2007) 5747-5752.

J.W. Morse, Am. J. Sci. 274 (1974) 97-107.

J.W. Morse, R.S. Arvidson, Earth-Science Rev. 58 (2002) 51-84.

J.W. Morse, R.S. Arvidson, A. Lüttge, Chem. Rev. 107 (2007) 342-381.

J. Moulder, W. Stickle, P. Sobol, K. Bomben, in Handbook of X-ray Photoelectron Spectroscopy (Ed: J. Chastain), Perkin-Elmer, Eden Prairie, MN, 1992.

J. Moulder, D. Hook, PHI Interface 17 (1997) 1-5.

S. Mukjerhee, M. Mukherjee, J. Electron Spectrosc. Relat.Phenom. 154 (2007) 90-95.

K. Muramatsu, T. Shimizu, N. Shinoda, A. Tatani, Chem. Econ. Eng. Rev. 16 (1984) 15-22.

W. Mönch, Solid State Commun. 58 (1986) 215-217.

H.W. Nesbitt, G.M. Bancroft, R. Davidson, N.S. McIntyre, A.R. Pratt, Am. Mineral. 89 (2004) 878-882.

M. Ni, B.D. Ratner, Surf. Interface Anal. 40 (2008) 1356-1361.

D.E. Nierode, B.B. Williams, Soc. Petroleum Eng. J. Trans. 251 (1971) 406-418.

C. Noiriel, L. Luquot, B. Madé, L. Raimbault, P. Gouze, J. van der Lee, Chem. Geol. 265 (2009) 160-170.

S. Oswald, S. Baunack, Surf. Interface Anal. 25 (1977) 942-947.

C.M. Pina, C. Pimentel, M. García-Merino, Surf. Sci. 604 (2010) 1877-1881.

L.N. Plummer, T.M.L. Wigley, D.L. Parkhurst, Am. J. Sci. 278 (1978) 179-216.

L.N. Plummer, D.L. Parkhurst, T.M.L. Wigley, in Chemical Modeling in Aqueous Systems (Ed: E.A. Jenne), ACS Symp. Ser. 93 (1979) 537-573.

O.S. Pokrovsky, J. Schott, F. Thomas, Geochim. Cosmochim. Acta 63 (1999) 3133-3143.

O.S. Pokrovsky, J.A. Mielczarski, O. Barres, J. Schott, Langmuir 16 (2000) 2677-2688.

O.S. Pokrovsky, J. Schott, Am. J. Sci. 301 (2001) 597-626.

O.S. Pokrovsky, J. Schott, Environ. Sci. Technol. 36 (2002) 426-432.

O.S. Pokrovsky, S.V. Golubev, J. Schott, Chem. Geol. 217 (2005) 239-255.

O.S. Pokrovsky, S.V. Golubev, J. Schott, A. Castillo, Chem. Geol. 265 (2009) 20-32.

B.E. Polig, G.H. Thompson, D.G. Friend, R.L. Rowley, W.V. Wilding, in Perry's Chemical Engineer's Handbook, 8th. ed. (Eds: R.H. Perry, D.W. Green), McGraw-Hill, New York, 2008, p. 2-122.

K. Puustinen, J.A. Karhu, Geol. Surv.Finland, Special pap. 27 (1999) 39-41.

M. Raines, T. Dewers, J. Petroleum Sci. Eng. 17 (1997) 139-155.

B.D. Ratner, D.G. Castner, in Surface Analysis – The Principal Techniques 2nd Edition (Eds: J.C. Vickerman, I.S. Gilmore), John Wiley & Sons Ltd, Singapore, 2009, pp. 47-112.

H.W. Rauch, W.B. White, Water Resour. Res.13 (1977) 381-394.

R.J. Reeder, in Reviews in Mineralogy vol. 11, Carbonates: Mineralogy and Chemistry (Ed: R.J. Reeder), Mineralogical Society of America, Washington DC, 1983, pp. 1–48.

D. Rickard, E.L. Sjöberg, Am. J. Sci. 283 (1983) 815-830.

H.M. Rietveld, J. Appl. Cryst. 2 (1969) 65-71.

J.D. Rimstidt, S.L. Brantley, A.A. Olsen, Geochim. Cosmochim. Acta 99 (2012) 159-178.

S. Rode, N. Oyabu, K. Kobayashi, H. Yamada, A. Kühnle, Langmuir 25 (2009) 2850-2853.

E. Rufe, M. F. Hochella Jr., Sci. 285 (1999) 874-876.

A.S. Rukhlov, K. Bell, Miner. Petrol. 98 (2010) 11-54.

E. Ruiz-Agudo, C.V. Putnis, C. Jiménez-López, C. Rodriguez-Navarro, Geochim. Cosmochim. Acta 73 (2009) 3201-3217.

E. Ruiz-Agudo, M. Urosevic, C.V. Putnis, C. Rodríguez-Navarro, C. Cardell, A. Putnis, Chem. Geol. 281 (2011) 364-371.

H. Rutto, Z. Siagi, M Mbarawa, J. Hazard. Mater. 168 (2009) 1532-1536.

R.D. Schlueter, in Synchrotron Radiation Sources: a Primer, Series on synchrotron radiation techniques and applications, vol. 1 (Ed: H. Winick), World Scientific Publishing Co Pte Ltd, Singapore, 1994, pp. 377-408

J. Schott, S.L. Brantley, D. Crerar, C. Guy, M. Borcsik, C. Willaime, Geochim. Cosmochim. Acta 53 (1989) 373-382.

J. Schott, O.S. Pokrovsky, E.H. Oelkers, in Reviews in Mineralogy & Geochemistry vol. 70, Thermodynamics and kinetics of water-rock interaction (Eds: E.H. Oelkers, J. Schott), Mineralogical Society of America, Washington DC, 2009, pp. 207-258.

M.P. Seah and W.A. Dench, Surf. Interface Anal. 1 (1979) 2-11.

P.M.A Sherwood, Surf. Sci. 600 (2006) 771-772.

S.-M. Shih, J.-P.Lin, G.-Y. Shiau, J. Hazard. Mater. B79 (2000) 159-171.

R. Shiraki, P.A. Rock, W.H. Casey, Aquatic Geochem. 6 (2000) 87-108.

D.A. Shirley, Phys. Rev. B 5 (1972) 4709-4714.

Z.O. Siagi, M. Mbarawa, J. Hazard. Mater. 163 (2009) 678-682.

K. Siegbahn, C. Nordling, A. Fahlman, R. Nordberg, K. Hamrin, J. Hedman, G. Johansson, T. Bergmark, S.-E. Karlsson, I. Lindgren, B. Lindberg, Nova Acta Regiae Societatis Scientiarum Upsaliensis IV, 20 (1967) 5-39.

A. Silva, R.M.F. Lima, V.A. Leão, J. Hazard. Mater. 221-222 (2012) 45-55.

E.L. Sjöberg, Geochim. Cosmochim. Acta 40 (1976) 441-447.

E.L. Sjöberg, Stockholm Contributions Geol. 32 (1978) 1-92.

E.L. Sjöberg, D.T. Rickard, Chem. Geol. 42 (1984) 119-136.

A.J. Skinner, J.P. LaFemina, H.J.F. Jansen, Am. Mineral. 79 (1994) 205-214.

S. Sommer, Am. Mineral. 60 (1975) 483-484.

G. Sposito, in Mineral-water interface geochemistry, Reviews in Mineralogy vol 23 (Eds: M.F. Hochella, Jr, A.F. White), Mineralogical Society of America, Washington DC, 1990, pp. 261-280.

R.K. Srivastava, W. Jozewicz, C. Singer, Envron. Prog. 20 (2001) 219-228.

S.L. Stipp, M.F. Hochella Jr., Geochim. Cosmochm. Acta 55 (1991) 1723-1736.

W. Stumm, Colloid Surf. A: Physicochem. Eng. Aspects 120 (1997) 143-166.

B. Sun, Q. Zhou, X. Chen, T. Xu, S. Hui, J. Hazard. Mater. 179 (2010) 400-408.

J. Söderström, N. Mårtensson, O. Travnikova, M. Patanen, C. Miron, L.J. Sæthre, K.J. Børve, J.J. Rehr, J.J. Kas, F.D. Vila, T.D. Thomas, S. Svensson, Phys. Rev. Lett. 108 (2012) 193005.

F.W. Tegethoff, J. Rohleder, E. Kroker (Eds.), Calcium Carbonate – From the Cretaceous Period into the 21st Century, Birkhäuser Verlag, Basel, Switzerland, 2001.

B.J. Tielsch, J.E. Fulghum, Surf. Interface Anal. 24 (1996) 28-33.

M. Tchaplyguine, Personal communication (2013).

J.O. Titiloye, N.H. de Leeuw, S.C. Parker, Geochim. Cosmochim. Acta 62 (1998) 2637-2641.

A. Trikkel, T. Kaljuvee, A. Soesoo, R. Kuusik, in Horizons in Earth Science Research Volume 7 (Eds: B. Veress, J. Szigethy), Nova Publishers, New York, 2012, pp. 147-196.

D.G. Truhlar, W.L. Hase, J.T. Hynes, J. Phys. Chem. 87 (1983) 2664-2682.

D.G. Truhlar, B.C. Garrett, S.J. Klippenstein, J. Phys. Chem. 100 (1996) 12771-12800.

M. Urosevic, C. Rodriguez-Navarro, C.V. Putnis, C. Cardell, A. Putnis, E. Ruiz-Agudo, Geochim. Cosmochim. Acta 80 (2012) 1-13.

P. Van Cappellen, L. Charlet, W. Stumm, P. Wersin, Gechim. Cosmochim. Acta 57 (1993) 3505-3518.

J.C. Vickerman, in Surface Analysis – The Principal Techniques 2nd Edition (Eds: J. C. Vickerman, I. S. Gilmore), John Wiley & Sons Ltd, Singapore, 2009, pp. 1-8.

A. Villegas-Jiménez, A. Mucci, O.S. Pokrovsky, J. Schott, Geochim. Cosmochim. Acta 73 (2009) 4326-4345.

M.D. Vinson, R.S. Arvidson, A. Lüttge, J. Cryst. Growth 307 (2007) 116-125.

M.D. Vinson, A. Lüttge, Am. J. Sci. 305 (2005) 119-146.

J.N. Walsh, in Modern Analytical Geochemistry: An Introduction to Quantitative Chemical Analysis Techniques for Earth, Environmental and Materials Scientists (Ed: R. Gill), Addison Wesley Longman Limited, Singapore, 1997, pp. 41-66.

J.M. Wampler, J.L. Kulp, inPetrologic Studies: a volume in honor of A.F. Buddington (Eds: A.E.J. Engel, H.L. James, B.F. Leonard), The Geological Society of America, New York, 1962, pp. 105-114.

P.L. Ward, Thin Solid Films 517 (2009) 3188-3203.

H.-R. Wenk, A. Bulakh, Minerals: Their constitution and origin, Cambridge University Press, Cambridge, 2008.

K.L. Williams, An introduction to X-ray spectrometry: X-ray fluorescence and electron microprobe analysis, Allen & Unwin, London, 1987.

H. Winick, in Synchrotron Radiation Sources: a Primer, Series on synchrotron radiation techniques and applications, vol. 1 (Ed: H. Winick), World Scientific Publishing Co Pte Ltd, Singapore, 1994, pp. 1-29.

M. Wolthers, L. Charlet, P. van Cappellen, Am. J. Sci. 308 (2008) 905-941.

V.P. Wright, in Carbonate Sedimentology (Eds: M.E. Tucker, V.P. Wright), Blackwell Science Ltd, Somerset, the UK, 1990, pp. 1-27.

G. Xiang, G. Rui-tang, D. Hong-lei, L. Zhong-yang. C- Ke-fa. J. Hazard. Mater. 168 (2009) 1059-1064.

J. Xu, C. Fan, H.H. Teng, Chem. Geol. 322-323 (2012) 11-18.

L. Zhang, A. Sato, Y. Ninomiya, E. Sasaoka, Fuel 82 (2003) 255-266.

ISBN 978-952-12-3161-2
Åbo Akademi